Physics – Uspekhi **52** (4) 315 – 334 (2009)

REVIEWS OF TOPICAL PROBLEMS

PACS numbers: **61.46.–w**, 61.72.Mm, **62.25.–g**

Strength of nanostructures

R A Andrievski, A M Glezer

DOI: 10.3367/UFNe.0179.200904a.0337

Contents

Abstract. **A state-of-the-art review is presented of research into the strength, the ductility, the superplasticity, and other mechanical properties of metal, alloy, intermetallic, semiconductor, and high-melting-point compound-based nanomaterials. Various theoretical approaches are described. Size effects, interfaces, and other structural factors are examined from the standpoint of their influence on the strength and plasticity of nanostructured materials. Some problems yet to be solved are pointed out.**

1. Introduction

The strength of materials is a critical problem in condensed matter physics, of primary importance for the development of new structural and tool materials. It is equally important for the creation of new-generation functional materials meeting requirements for carrying capacity and resistance to catastrophic failure. Extensive studies in the field of nanoscale material science initiated 15–20 years ago have from the very beginning been focused on the strength of nanostructures, because these have proven to be very strong (hard) and nonplastic. Simultaneously, it has been realized that the traditional dislocation approach to explaining the main patterns of their mechanical behavior must be modified.

The regularities and mechanisms of nanostructure influence on the strength and ductility characteristics have been elucidated in numerous investigations, whose results are reported in many papers, reviews, and monographs. More than 25 of the most important publications over the last 10 years are listed in [1–27]. We believe that the most comprehensive analysis of the mechanical properties of nanoscale materials is presented in [15]. Notwithstanding this voluminous information, our knowledge of the mechanical behavior of nanostructures remains incomplete for the lack of data on fracture toughness, creep, superplasticity, and other properties of metal-based nanomaterials, including those that contain a brittle phase. In the present review, consideration of these issues is preceded by a concise description of the structural features of nanoscale materials having a marked effect on their strength and plasticity. As accepted in the current literature [2, 3], nanoscale materials are understood as objects with a characteristic size of structural elements below 100 nm.

2. Structural features

2.1 Point and line defects

It is known that the concentration of thermal vacancies in a metal object is normally close to 10^{-4}, even near the melting point. Nanostructures containing less than 10^4 atoms (clusters, single nanoparticles, nanofilms, and nanowires) can hardly be expected to have vacancies in thermal equilibrium, especially at room temperature [12]. The radius of gold particles lacking vacancies at 600 K was estimated to be 10 nm or less. Moreover, it was shown in [28] that the activation energy of thermal vacancies in metal nanoparticles increases with decreasing the radius.

These facts about thermal vacancies are important for the consideration of diffusion processes and creep phenomena in isolated nano-objects, but they are irrelevant to consolidated (bulk) nanomaterials composed of many strongly bonded

---

R A Andrievski Institute of Problems of Chemical Physics,
Russian Academy of Sciences,
prosp. akad. Semenova 1, 142432 Chernogolovka,
Moscow region, Russian Federation
Tel. (7 496 52) 277 93
Fax (7 496 52) 235 07
E-mail: ara@icp.ac.ru
A M Glezer Kurdyumov Institute for Physical Metallurgy,
Bardin Science Center for Ferrous Metallurgy,
2-ya Baumanskaya ul. 9/23, 105005 Moscow, Russian Federation
Tel. (7 495) 777 93 50
Fax (7 495) 777 93 50
E-mail: glezer@imph.msk.ru

Received 6 October 2008, revised 22 December 2008
Uspekhi Fizicheskikh Nauk **178** (4) 337 – 358 (2009)
DOI: 10.3367/UFNr.0179.200904a.0337
Translated by Yu V Morozov; edited by A M Semikhatov

nanocrystals. Nevertheless, structural vacancies in the metal and nonmetal sublattices[1] of nonstoichiometric compounds (nitrides, oxides, sulfides, borides, etc.) can affect lattice dislocation motion and the manifestation of nondislocation modes in deformed solids [30]; true, direct experimental evidence of such influence in relation to nanoscale materials is still unavailable.

Also, it should be borne in mind that the use of methods such as high-energy ball milling and megaplastic (intense) deformation (MPD) may significantly increase the concentration of vacancies and other defects in nanostructures as evidenced by markedly enhanced diffusibility and the formation of supersaturated solid solutions (see [12, 14, 20, 31]).

Attempts to consider dislocations in nanostructures (by analogy with conventional crystals) as the main carriers of plastic deformation have been reported in many publications and can be arbitrarily categorized as follows:

- experimental studies by transmission and scanning electron microscopy (TEM and SEM, respectively) including high atomic resolution techniques (HRTEM and HRSEM) and in situ studies within the TEM and/or SEM columns;
- theoretical estimates of dislocations in nanostructures;
- computer simulation of deformation processes, largely by molecular dynamics methods.

Elucidation of the structural mechanisms of plastic deformation in nanostructured materials is based on the results obtained in studies along these three lines.

As is known [3, 12], the limited number of dislocations in nanoparticles, nanofilms, and nanocrystals is due to the influence of at least two factors. First, the characteristic size L in these objects can be smaller than the Frank–Reed loop as a major source of dislocations: $l_{\mathrm{FR}} = Gb/\tau_{\mathrm{cr}}$, where G is the shear modulus, b is the Burgers vector, and τ_{cr} is the critical shear stress. At typical values $G/\tau_{\mathrm{cr}} = 10^2 - 10^4$ and $b \sim 0.2$ nm, l_{FR} is 20–200 nm; this means that no multiplication of dislocations by the Frank–Reed mechanism occurs at $L < l_{\mathrm{FR}}$. Second, image forces arising at interfaces tend to push dislocations out from nanocrystals, this effect being hindered by friction forces within the crystal lattice. According to [32], the minimal characteristic size of dislocation stability L^* below which the probability of dislocations is low can be expressed as $L^* = aGb/2\tau_{\mathrm{P}}$, where $a = 0.1 - 1.0$ is a coefficient depending on the dislocation geometry (τ_{P} is the Peierls stress). For edge dislocations in copper, nickel, iron, and titanium nitride, L^* is respectively 25, 10, 2, and 1 nm, i.e., roughly equal to experimental values. Figure 1 presents an HRSEM image of a TiN film [33]. A few edge dislocations are clearly seen inside the nanocrystallite measuring around 10 nm, in agreement with theoretical estimates [32].

An important source of dislocations in nanoscale materials is their emission from grain boundaries under deformation observed experimentally and predicted theoretically or by computer simulation [6, 11, 13, 15, 19, 26, 34–36]. For example, a simulation experiment demonstrated the broadening of intergrain boundaries and the appearance of Shockley partial dislocations connected by a stacking fault [36]. The fragment of interest contained 16 nanograins ($\sim 10^5$ atoms). Today, larger three-dimensional objects, e.g., containing 125 nanograins with several million atoms, are used in computer experiments (see Section 3.1).

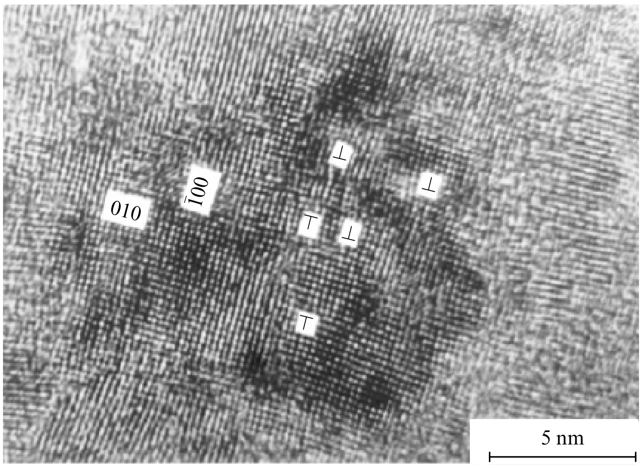

Figure 1. High-resolution image of a TiN film [33].

Lattice dislocation density in nanostructures may be higher than 10^{11} cm^{-2}; equally large are microdistortions resulting from atom displacements in crystal lattice corners. To be fair, the aforesaid mainly refers to metal-based materials obtained by the MPD method [4, 7, 18, 21].

Deformation of nanoscale materials may give rise to one more type of linear defects, rotational disclinations (see Section 3.2).

2.2 Interfaces. Triple junctions. Twins

The small size of structural elements in nanomaterials is responsible for the important role of interfaces (intercrystallite and interphase boundaries). It is easy to show that the interface fraction in the bulk is $\sim 6s/L$, where $2s$ is the boundary width (boundary zone), usually accepted to be around 1 nm. In other words, the fraction increases significantly from 0.3% to 3% and 30% at the respective crystallite size 10^3, 10^2 (the conventional upper limit L for nanostructured materials), and 1 nm. For nanomaterials, the increasing number of triple junctions must be taken into account, in addition to grain boundaries. Figure 2 shows volume fractions of different interface components depending on the grain size in a single-phase material [37]. Although

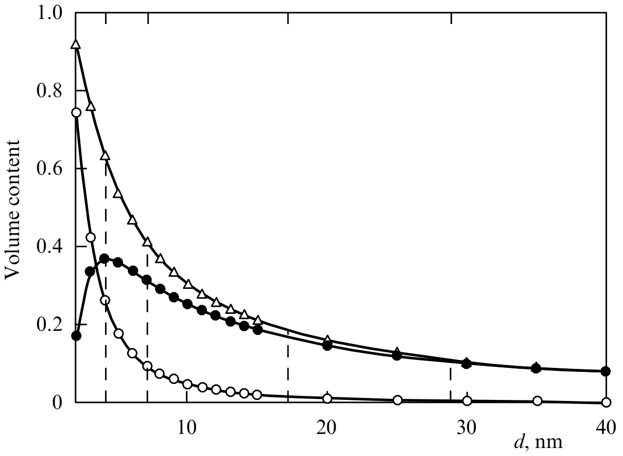

Figure 2. Volume content of common interfaces (△), intergrain boundaries (●), and triple junctions plotted versus the grain size [37].

---

[1] The specific features of interstitial phase nanoscale films of sub- and superstoichiometric composition are reviewed in [29].

Fig. 2 includes only estimated data, they give evidence of a rapid increase in the number of triple junctions with decreasing L. It was calculated in [8] that triple junctions can have a marked effect on diffusibility, dislocation nucleation, and the rotational deformation mode in nanoscale materials.

The structure of intergrain boundaries was thoroughly studied by the MPD technique [17, 18, 21]. Most intergrain boundaries in objects with the grain size 100 nm or more are believed to be large-angle boundaries characterized by high specific surface energy. It is therefore assumed that they have some peculiar features, such as a high concentration of free volume and grain-boundary dislocations, enhanced diffusive permeability, and a tendency toward segregation [18, 21].

Peculiarities of the interface structure and stressed state in thin single- and multilayer films (the so-called 'superlattices') have been analyzed in [38–40].

Planar defects of another type are twins, most frequently formed as a result of growth and deformation in metals and alloys with a face-centered cubic (FCC) lattice. Twin structures have gained the attention of material scientists [15, 16, 25, 26] since the results of [41, 42] became available. It was shown using copper samples obtained by pulsed electrochemical deposition that both strength and plasticity substantially increase as the twin lamella thickness decreases [41]. Figures 3a–c show light-field TEM images of these samples along with their crystallite and lamella size distributions; Fig. 3d presents the results of mechanical tests. It can be seen that the strength and ductility of the samples having a nanotwin structure (A, B, C) are significantly greater than those of nanocrystal samples fabricated by conventional technology. Also, it is evident that sample C, which is much stronger than ordinary copper (over 4 times in terms of the ultimate stress limit and by a factor of 18 in terms of the elastic limit), exhibits fairly good plasticity (relative elongation $\delta \sim 14\%$).[2] It is worth noting that interlamellar boundaries do not present barriers to traveling electrons. Indeed, samples A, B, and C are not different from conventional copper in terms of electric conductivity [41]; this fact is of great importance for the development of highly wear-resistant electrotechnical materials.

3. Size effects

3.1. Hall–Petch relation. Plasticity

Hundreds of studies have been devoted to the mechanical properties of nanostructures. Many of them were aimed at elucidating the applicability to nanoscale materials of the known Hall–Petch (HP) relation between the yield strength σ_{y} and hardness H for a polycrystalline materials with grain size L,

$$\sigma_{\mathrm{y}} = \sigma_0 + K_{\mathrm{y}} L^{-1/2}, \quad H = H_0 + K_{\mathrm{HP}} L^{-1/2}, \tag{1}$$

where K_{y} and K_{HP} are the HP coefficients and σ_0 and H_0 are constants associated with monocrystal yield strength and hardness [22]. In the most popular theoretical interpretation of empiric relations (1), boundaries are regarded as obstacles for shear displacement from one grain to another. Nanosize grains experience not only a shortage of dislocations (as mentioned in Section 2.1) but also the impossibility of their formation for realizing the 'relay' mechanism.

In this section, we analyze only those recent findings that illustrate the effects of crystallite size (size effects) on strength and plasticity at room temperature.

Figures 4 and 5 (except 4d and 5a) present experimental data in HP coordinates for bulk nanomaterials, films, layers, and small compacts [44-48]. Plots in Fig. 4 summarize the data on three metals (Ni, Au, Ag) [44, 45] obtained by many authors; Fig. 5 presents data on superhard BN-based nanocomposites [46], nickel aluminide [47], and nitride films [48]. It can be seen from these results that deviations from the standard HP dependence (1) occur practically in all cases in the nanometer range ($L^{-1/2} > 0.1$ nm$^{-1/2}$ or $L < 100$ nm). This situation is most thoroughly described for metals as variations of the HP coefficients. A detailed analysis of research carried out by Russian authors using samples obtained by MPD and crystallization from the amorphous state is presented in [7, 18]. Hardness changes in multilayer metal nanocomposites of the Cu–Nb and Nb–(Nb–50% Ti alloy) types are considered in [49, 50]. Nanolaminates were fabricated by an original method of multiple rolling of alternating layers. It turned out that the HP relation is satisfied in the layer width range from 5 to 380 nm, but its coefficients vary considerably when each layer is about 20 nm thick.

The author of [44] proposes considering the dependence $\sigma_{\mathrm{y}} = f(L^{-1/2})$ for three size intervals: I, $L \gtrsim 1$ μm; II, $L \sim 10-1000$ nm; and III, $L \lesssim 10$ nm (see Fig. 4). The third interval is characterized by saturation of the change in the yield strength (hardness) and even by the change of the HP coefficient sign and a decrease in σ_{y} and H with decreasing the crystallite size. This interval is referred to as the inverse HP or 'anti-HP' dependence. It is assumed that the dislocation activity in this interval is absent and the deformation is due to other mechanisms. Inflection of the dependences $\sigma_{\mathrm{y}} = f(L^{-1/2})$ is related to the effect of boundary segregations associated with annealing of nanostructures, as is clearly seen in Fig. 5b and discussed at greater length for other nanostructured materials in [47]. On the other hand, the essentially nonmonotonic and irregular alteration of hardness in two varieties of brittle cubic boron nitride-based compacts (Fig. 5a) obtained at high pressure and temperature can be explained in the framework of quantum confinement effects [46].

It should be borne in mind that the discussion of the plots in Figs 4 and 5 requires an analysis of the relevance of these data to the influence of the size effect 'in its pure form' in order to exclude other factors, such as the residual stress, twins, and grain size distribution. Figure 5 shows the effect of the residual compressive stress (c) and crystallite size (d) on the hardness of TiN and CrN films [48].

Evidently, these parameters have a concerted effect. Finally, the crystal size distribution also plays an important role in the formation of nanoscale material properties. With regard to deformation processes (including superplasticity and creep), this problem was addressed in [45, 51, 52]. The nanocrystallite distribution is assumed to have a log-normal form

$$f(L,S) = \frac{1}{(2\pi)^{1/2} SL} \exp\left[-\frac{1}{2}\left(\frac{\ln(L/L_{\mathrm{m}})}{S}\right)^2\right], \tag{2}$$

where L_{m} is the median distribution size and S is the standard deviation or dispersion of the distribution (the

---

[2] It was shown in [168] following [41, 43] that further thinning of twin lamellae leads to a strength decrease; that is, the strength shows a nonmonotonic dependence on the lamella width with a maximum at 15 nm.

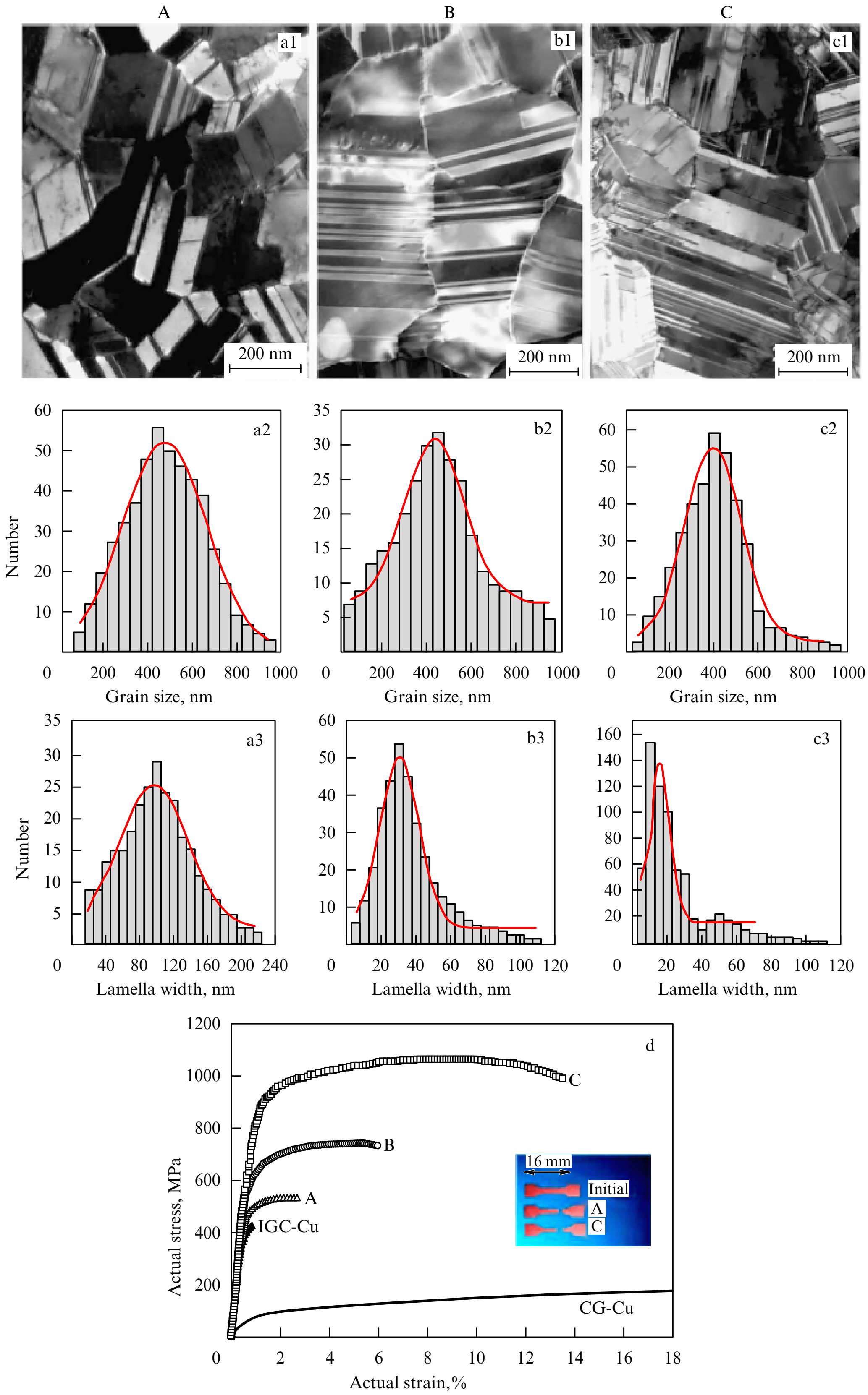

Figure 3. Structure and mechanical properties of nanotwin copper samples A, B, and C: (a1, b1, and c1) TEM images; (a2, b2, and c2) crystal size distribution; (a3, b3, and c3) size distribution of twin lamellae width [43]; (d) diagram of the uniaxial tension of A, B, C samples and copper samples with an ordinary nanocrystalline (IGC-Cu) and macrocrystalline (CG-Cu) structure [43].

mean quadratic error for the grain size distribution). Also, it is easy to show that an increase in S (i.e., a size distribution expansion) shifts the distribution toward smaller values [52].

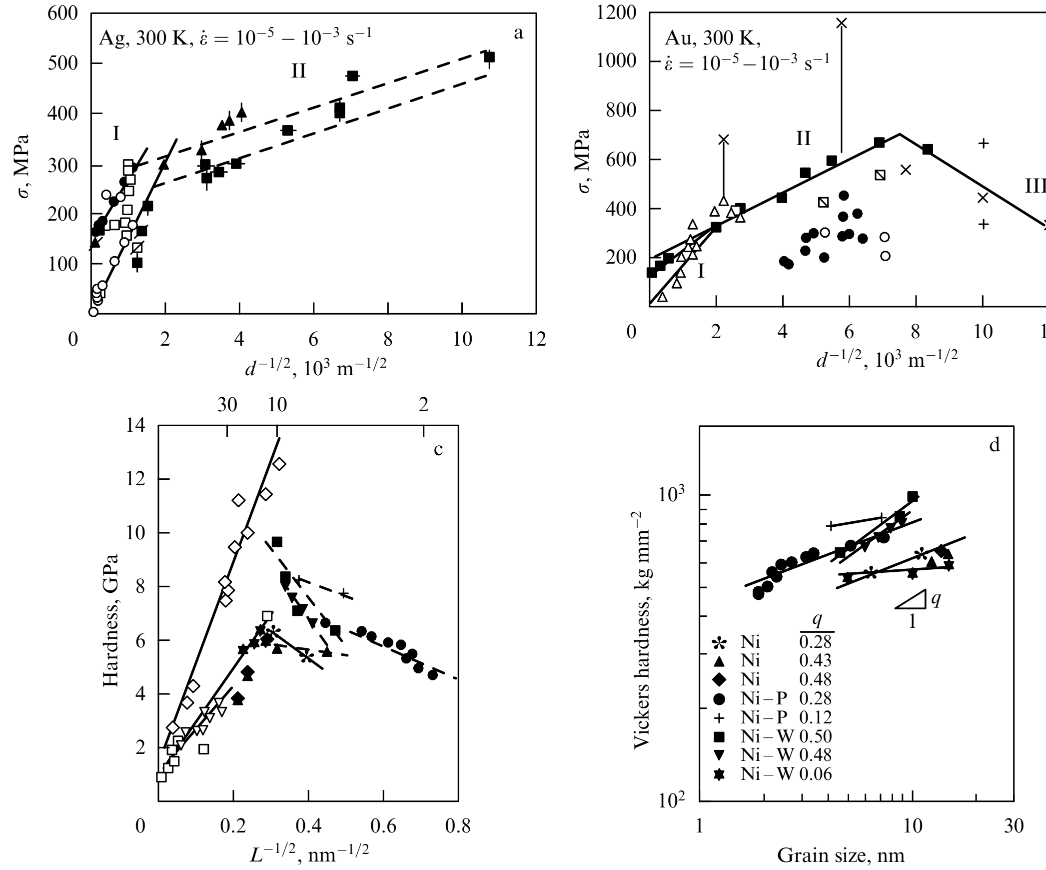

Figure 4. Grain size dependence of silver (a) and gold (b) strength [44]; nickel hardness in the size range from 2 nm or more (c) and less than 10 nm (d); q, the exponent in the relation $H \sim L^q$ [45]. Points in Figs c and d are data from different authors.

The authors of [45] analyzed hardness variations for nanocrystalline nickel in a wide range of sizes (up to 2 nm) and assumed diffusion creep along grain boundaries for $L < 10$ nm (Fig. 4c, d). Based on these data, they considered the effect of standard deviation on the inflection point of the dependence $\sigma_y = f(L^{-1/2})$ and on the exponent of the descending slope of the plot for this dependence ($H \sim L^q$, $q > 0$). It was shown that the wider the grain size distribution, the greater the inflection point displacement toward smaller sizes (in agreement with [52]) and the steeper the decrease in hardness within this interval (i.e., q increases) [45].

The results in [52] are important in that the authors considered other possible mechanisms of grain-boundary softening, besides diffusion creep, and analyzed the effect of S not only on the yield strength but also on the ultimate stress limit and homogeneous deformation until a neck develops. These data are of enormous interest in that they suggest an enhancement of the nanomaterial resistance to neck formation (up to 5–10% at $S > 0.8$) with increasing dispersion. These values are considered acceptable for practical application purposes. Thus, a wider grain size distribution is likely to promote an improvement in plastic characteristics, even if it somewhat decreases the strength.

The structural optimization of nanomaterials to improve their strength while sacrificing very little ductility (i.e., the ability to deform without fracturing) is the quintessence of extensive research in the field of nanoscale material science [16, 53]. Ni, Fe, Ti, and many other metals except Zn, Co, and Cu are characterized by very small relative elongation coefficients in the nanocrystalline state. In addition, they are very strong but lack plasticity (Fig. 6 [53]). The activation volume v^* decreases with a decrease in the crystallite size in FCC metals,

$$v^* = b\xi l^* , \tag{3}$$

while the strain-rate sensitivity exponent m of flow stress increases:

$$m = \left(\frac{\partial \ln \tau}{\partial \ln \dot{\varepsilon}}\right)_T = \frac{k_B T}{\tau v^*} . \tag{4}$$

Here, ξ is the barrier width, l^* is the distance between forest dislocations, τ is the flow stress, $\dot{\varepsilon}$ is the strain rate, k_B is the Boltzmann constant, and T is the deformation temperature [15, 22]. For example, as the grain size decreases from 100 to 20 nm, v^* decreases roughly threefold from $\sim 30\,b^3$ and m increases by a factor of 2 from ~ 0.02 [26]. For conventional FCC metals, $v^* \sim (10^2 - 10^3)\,b^3$ (plastic deformation) and $m = 1$ (diffusion creep).

Apart from the aforementioned low dislocation activity typical of nanostructures at $L < L^*$, the decrease in strength and plasticity is promoted by the presence or development of cracks (pores) at the interfaces. Nickel strain diagrams obtained in a computer experiment show the flow stress 3.5 and 4.5 GPa for crystallites measuring 5 and 8 nm (a sample of 125 grains respectively containing 1.2×10^6 and 4.6×10^6 atoms) [57] (see also Figs 4c, d). Visualization of fracture patterns revealed preferential accommodation of nanocracks at intercrystallite boundaries (intercrystallite break-up processes are discussed in

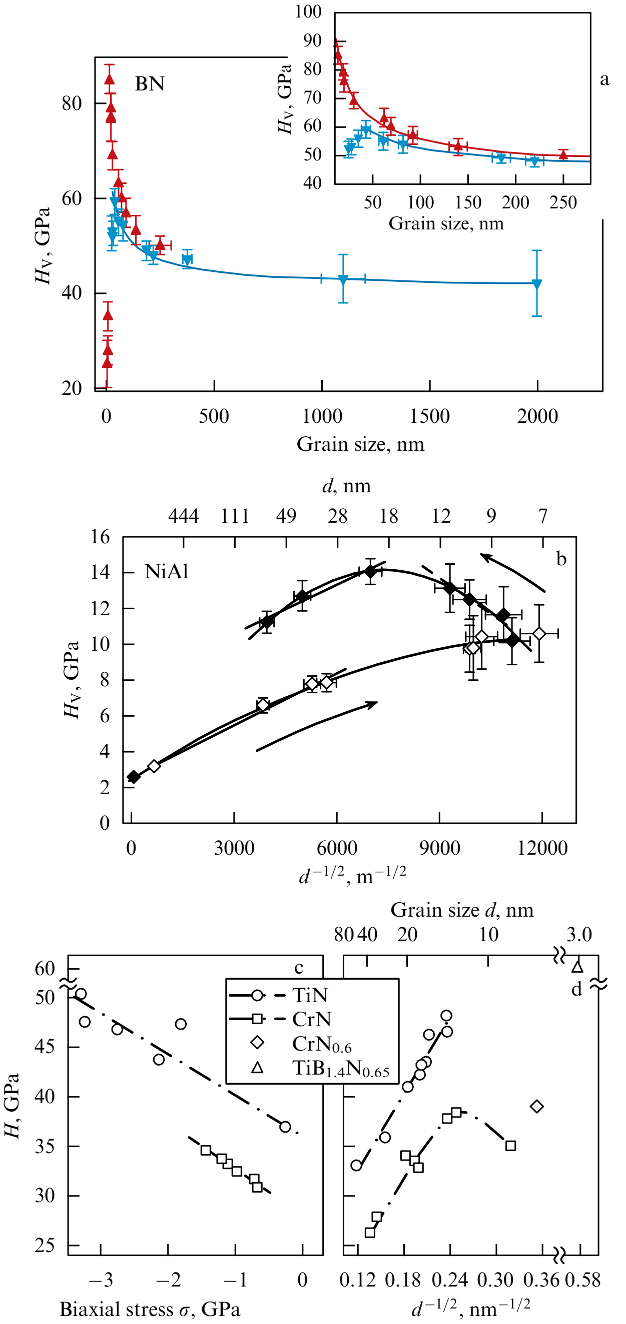

Figure 5. Effect of the grain size on boron nitride hardness (H_V, Vickers hardness) (a): ▲, aggregated BN composites; the ▼ and the lower curve in the inset, cubic BN [46]; (b) the same for nickel aluminide: ◆, after annealing; ◇, before annealing [47], and nitride films (d); (c) effect of residual compressive stress [48].

Section 3.2). These boundaries have a plastisizing effect as they facilitate intercrystallite sliding (grain-boundary microslip) and serve as barriers to intracrystallite crack propagation and dislocation emission.

Eight major approaches to the enhancement of plasticity in metal and alloy-based nanostructured materials are listed in [16]: (1) creation of bimodal structures to which the nanocrystal matrix imparts high strength while larger inclusions promote plasticity [58]; (2) preparation of multiphase compositions; (3) formation of twin structures (see Fig. 3 [43]); (4) fabrication of dispersely hardened alloys; (5) the use

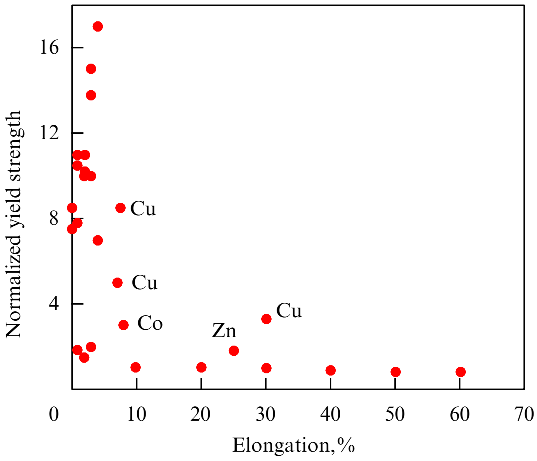

Figure 6. Relation between the normalized yield strength (with respect to that for conventional coarse-grained metals) and the relative elongation for nanoscale metals [53].

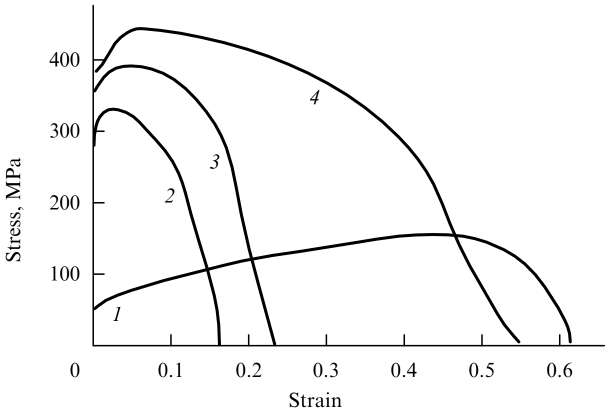

Figure 7. Stress–strain curves for copper samples: *1*, the starting coarse-grained copper; *2*, the same after cold rolling; *3* and *4*, the same after 2 and 16 ECAE passes, respectively [59].

of transformation-induced plasticity (TRIP) and twining-induced plasticity (TWIP) effects; (6) low-temperature dynamic annealing; (7) increase in the strain-rate sensitivity exponent of flow stress m up to values inherent in superplastic alloys ($m \sim 1$) including multiple MPD treatment [21, 59]; (8) consolidation of nanoscale materials to ensure the absence of pores and microimperfections that tend to neutralize the positive effect of the nanostructure by generating stress concentrators.

The applicability of some of these approaches to nanomaterials is debatable. Nevertheless, the effectiveness of those itemized under Nos 1, 3, 7, and 8 has already been confirmed in experiment. For example, copper samples based on a nanostructured matrix with the grain size 80–200 nm (75 vol%) and 1–3 μm inclusions (25 vol%) exhibited good strength ($\sigma_y = 400$ MPa) and ductility (relative elongation $\delta = 65\,\%$) characteristics [58]. Figure 3d demonstrates the excellent properties of copper samples for which density variations depending on the twin lamellae thickness obey the HP relation [43]. Figure 7 shows the dependences $\sigma = f(\varepsilon)$ for copper samples of different origins [21, 59]. It can be seen that strength and ductility increase as the number of equal-channel angular pressing (ECAP) passes increases; the

Table 1. Structural and deformational characteristics of copper and bronze (10 mass% Zn) samples.

Object	γ_{sf}, mJ m^{-2}	L, nm		σ_{y}, MPa	δ, %		$\rho_{\mathrm{dis}} \times 10^{-10}$, cm^{-2}		φ, %	
		TEM	XSA		RE	UE	Ini	Fin	Ini	Fin
Copper	78	~ 180	~ 70	420	5.1	2.2	2.3	2.8	0.1	0.1
Bronze	35	~ 110	~ 50	580	7.1	3.8	5.9	7.3	4.8	5.5

Note: ρ_{dis}, dislocation density; φ, the probability of finding a twin between two planes (111); RE, the relative elongation before destruction; UE, the uniform elongation prior to neck development; Ini, initial state; Fin, final state after the tensile test.

strain-rate sensitivity exponent of flow stress also increases and the grain size distribution significantly extends. These promote an improvement in plasticity as noted above in discussing the results in [52]. The use of different consolidation techniques for nanoscale copper powders allowed obtaining practically nonporous nanostructured specimens (Fig. 6).

Theoretical treatment of strength and ductility properties of bimodal nanostructures (a nanocrystalline matrix with greater-size microinclusions, as in the experimental study [58] above) is presented in [24, 60–62]. The deformation behavior of such objects (assumed to be two-phase entities [61, 62]) under stretching tension was computed from additive considerations by the rule of mixtures

$$\sigma(\varepsilon) = (1 - f)\,\sigma^{\mathrm{n}}(\varepsilon) + f\sigma^{\mathrm{m}}(\varepsilon)\,, \qquad (5)$$

where f is the volume fraction of microinclusions and σ^{n} and σ^{m} are the strengths of unimodal nano- and microstructures. The 'two-phase' approach (grain body + interfaces) is very popular among nanomaterial scientists; its detailed analysis with regard to plastic and elastic properties is presented in [8, 10].

A comparison of the effectiveness of the approaches described in [60–62] is complicated by a variety of assumptions made by the authors. The difference between them lies in the postulated strain mechanisms for unimodal nanostructures (see formulas (6)–(8) below) and the distribution of plastic deformation between structural components. Although these approaches are qualitatively similar to those used in [58], their quantitative predictive value needs to be further improved.

An interesting aspect in [24] is the stereological analysis of two-phase nanomaterials of a composite nano- and micro-scale structure that extends the known classification of nanomaterials proposed by Gleiter [2]. Other classifications are available including some that postulate as many as 36 variants in nanostructure [63].

There are other approaches to increasing the nanocrystal plasticity besides those described in the preceding paragraphs. For example, the same goal can be achieved by varying the stacking fault energy γ_{sf}, which is known to determine the probability of formation of partial dislocations and twins [64]. This effect was demonstrated by comparison of the deformation characteristics of structurally attested copper and bronze samples fabricated by the MPD technique (high-pressure torsion) with subsequent cold rolling (Table 1) [65].

These data indicate that bronze samples with a low stacking fault energy are characterized by higher strength, ductility, and dislocation-twining activity. The authors of [65] attribute the difference between the L values obtained by the TEM and X-ray diffraction (XRD) analysis to the fact that the latter method measures the size of coherently scattering structures. It is important, however, that identical MPD regimes reveal a more disperse structure in bronze samples having a higher strain-rate sensitivity exponent. Computer experiments [11] also showed high dislocation activity in nanocrystalline FCC metals with a low stacking fault energy.

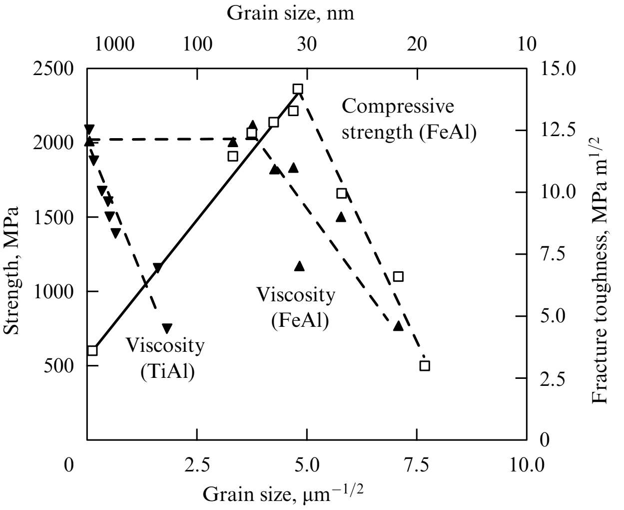

Figure 8. Variations of compressive strength in FeAl and fracture toughness in FeAl and TiAl depending on the grain size (samples were fabricated by hot isostatic pressing of milled powders) [66, 69].

Intrinsically fragile materials (intermetallides, semiconductors, high-melting-point compounds, amorphous alloys, etc.) deserve special mention. As noted in [3, 66], the optimism of the authors of [67] provoked by the observation of the high indentation compliance of CaF_2 and TiO_2 proved unwarranted in relation to the possibility of increasing the plasticity of bulk nanoceramic materials by virtue of diffusional creep at room temperature.[3] As shown in Fig. 8, the strength of aluminides increases in accordance with the HP relation up to the grain size ~ 30 nm and then decreases [66, 69]. The decrease is attributable to the residual porosity effect and imperfection of interparticle contacts. Fracture toughness diminished in the tested size range.

Nevertheless, nanoscale films, wires, inclusions, and other nanoobjects display residual plastic deformation. Figure 9 depicts fractures near indentation imprints in a TiN film having a clear-cut columnar structure. Individual columns are obviously bent by nonuniform bulk compression (Fig. 9a); in many cases, such deformation results in brittle fragmentation (Fig. 9b). The difference is due to the sliding of the

---

[3] The schemes illustrating a decrease in the dislocation activity in metals and an increase in intergrain sliding (i.e., increase in plasticity) in brittle objeats as the grain size decreases are given in [68].

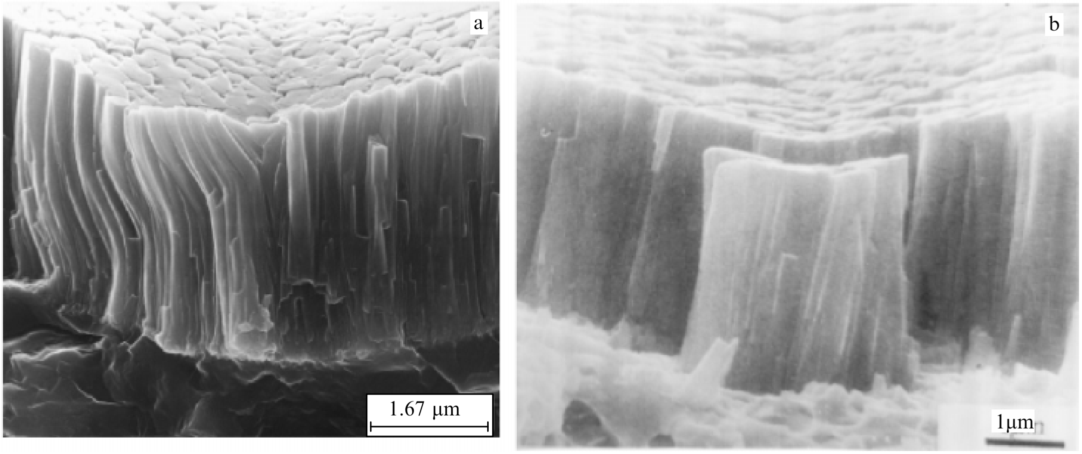

Figure 9. Fractogram of a TiN film near the indenter puncture: (a) residual plastic deformation of several TiN columns, (b) brittle fragment (images obtained by HRSEM) [33, 70].

columns against each other, i.e., to conditions at the interfaces between them. On the other hand, manifestations of plastic deformation may reflect the presence of dislocations inside the columns (Fig. 1).

Plastic deformation in monocrytalline β-SiC and Si wires less than 70–100 nm in diameter was documented by in situ observation of their bending and stretching in TEM and SEM columns [71–73]. The $\langle 110 \rangle \{111\}$ slip systems proved typical of FCC materials. Diametral and longitudinal deformations in these experiments were as great as 425% and 125%, respectively, (for Si, $T \sim 20\,^{\circ}\mathrm{C}$); the diameter decreased two-fold and the length by more than 200% (for SiC, $T \leqslant 80\,^{\circ}\mathrm{C}$). The dislocation density increased in the initial phase of the deformation and amorphization of the structure occurred in the deformation zone at the final stage.

Understanding the nature of plastic deformation in nanoparticles was greatly promoted by a series of research into amorphous nanocrystalline composites [74–76]. Controlled annealing was used to induce crystallization in the matrix of an amorphous $\mathrm{Fe_{58}Ni_{25}B_{17}}$ alloy and thereby produce the body-centered cubic (BCC) phase of Fe–Ni. The size (from 10 to 20 nm) and volume fraction (from 5 to 20%) of nanoparticles was varied by the choice of the appropriate thermal regime. Microindentation of the amorphous matrix created strongly localized shear bands, and their interactions with nanoparticles were studied by TEM from many perspectives. Four variants of interaction were identified, specifically, bending of shear bands around nanoparticles, decelaration of shear bands on isolated nanoparticles, intersection of nanoparticles by shear bands, and elastic accommodation effects when shear bands cause elastic deformation of the particles and give rise to secondary bands behind nanoparticles [74]. It has been shown in experiment [76], in excellent agreement with the theory [75], that the size of the particles determines which interaction mechanism operates in one case or another. As the size increases, the dominant interaction mechanism successively changes from the first to the fourth. Three important points must be mentioned. First, the interaction has a probabilistic character and depends on many factors, besides the particle size (the shear band width and propagation rate, the band–particle mutual orientation, the band shape, etc.). Second, the intersection of nanoparticles by shear bands gives unambiguous evidence of the possibility of dislocation flow (or its close analog) in particles, but this flow sharply decreases when the particles are less than 80 nm in size. Third, the results appear to be equally valid, albeit with certain reservations, for nanoparticles formed not in an amorphous matrix but in a crystal.

At this point, reference to the results of a computer experiment [77] is in order. This experiment showed that the deformation of nanocrystalline ($L = 8$ nm) cubic silicon carbide (β-SiC) at the first stage of stress application is mediated through intergrain sliding followed by an intragrain dislocation slide.

We note that the size of fragile nanoscale objects (TiN, SiC, Si $(\mathrm{Fe,Ni})\mathrm{B}_x$) [33, 70–76] in which plastic flow was recorded is consistent with estimates reported in [32]. Methods for in situ observation of dislocations in nanoscale objects as well as computer experiments are finding an increasingly wider application in current research as reflected in the ambitious program of the recent conference on *Emerging Methods for Understanding Mechanical Behavior. Imaging Methods: TEM, SEM, AFM, Moire* (2008 TMS Annual Meeting, New Orleans, LA, USA, March 9–13, 2008). In this country, in situ observations of deformation of nanoscale alloys based on Al (FCC), Fe (BCC), and Ti (HCP or hexagonal close packed structure) in a TEM column were described in [7, 78]. These studies demonstrated the active development of rotational deformation modes in nanocrystals less than 30 nm in size.

Measurement of film hardness is essential to gain a better understanding of the nanostructure strength. The present state of the art as regards single- and multilayer nanoscale films prepared from high-melting-point compounds is reflected in reviews [29, 38, 48, 79, 80] and a volume of collected articles [81]. We note that the hardness of multilayer structures of the $A\mathrm{N}/B\mathrm{N}$ and $C/B\mathrm{N}$ type (AN and BN are transition metal nitrides, C is metals like Cu, Ni, Mo, Nb) varies with the layer thickness (from 1–2 to ~ 100 nm); this behavior is described by a dependence with a maximum and substantially deviates from the rule of mixtures (see Fig. 17 below). It is attributed to peculiarities of dislocation and crack propagation across interphase boundaries. However, the large hardness of these objects is due not only to their nanostructure but also to other factors, such as residual stress (Fig. 5c).

3.2 Mechanisms of deformation and destruction

We consider and critically discuss proposed mechanisms of deformation and breakup of nanostructured materials. Their interpretations as of 2000 were reviewed in our paper [3]. To various degrees, this problem of plastic deformation usually preceding destruction is addressed in several recent reviews and monographs (see, e.g., [4–5, 17–22, 24–27]).

A starting point for understanding the nature of plastic deformation in nanocrystals was paper [82] in which athermal grain-boundary microshuffling was for the first time postulated as the principal mechanism of plastic flow under the action of high shear stress, an alternative to the classical dislocation flow at a low temperature. This concept was further extended in [6, 30]. In the framework of this model, the stress–strain (ε) relation has the form

$$\sigma_{\mathrm{y}}(\varepsilon)=\sigma_{\mathrm{s}}+AG\left(\frac{L}{L'}\right)\frac{\varepsilon}{qhn^2}\,,\quad \varepsilon<\varepsilon^*=nqh\left(\frac{2s}{L}\right)\gamma^*\,, \tag{6}$$

$$\sigma_{\mathrm{y}}(\varepsilon)=\sigma_{\mathrm{y}}(\varepsilon^*)+\alpha G\left(\frac{kb\varepsilon}{n\zeta L}\right)^{1/2}\,,\quad \varepsilon>\varepsilon^*\,, \tag{7}$$

where $A=\pi(2-v)/4(1-v)$, v is the Poisson coefficient, G is the shear modulus, σ_{s} is the shear stress at the flat grain boundary, L' is the mean size of the grain-boundary microsliding region, $2s$ is the boundary width, γ^* is the fracture energy, n is the mean orientation factor, and q, h, α, k, and ζ are numerical parameters [6]. At the initial stage of deformation ($\varepsilon<\varepsilon^*$), the shear is realized through shuffling at selected grain-boundary sites. Grain disclination rotation and the formation of dislocations are the main accommodation processes at this stage. Thereafter ($\varepsilon>\varepsilon^*$), dislocations are emitted from the boundaries into the interior of the grains.

The classical dislocation flow is gradually exhausted as the grain size in the nanocrystalline ensemble decreases, giving way to grain-boundary microsliding: the smaller the grain size, the easier it is for the sliding to proceed. It is the main cause of the anomalous behavior of the HP relation. This mechanism was further clarified in detail for bimodal structures with the smallness of the grain-boundary deformation taken into account [24].

The validity of this model was confirmed in many direct and computer experiments [17, 36]. Grain-boundary microsliding is especially efficacious in nanocrystals fabricated by amorphous state annealing, which gives rise to amorphous interlayers between grains, where the anti-HP effect is most explicitly pronounced [3].

In a similar model analyzed in [83], the plastic shear in nanoscale materials with the direct and inverse HP effect is considered with regard to a relay mechanism in which the dislocation (translational) mode is realized via grain-boundary shuffling and the rotational (disclination) mode via processes inside the grains and at their boundaries. It is shown that the transition from translational to rotational deformation and back explains the inverse HP effect.

Many researchers still seek to interpret the mechanical behavior of nanocrystals in the framework of classical dislocation concepts. These models may be useful for describing plastic flow in 'large' nanocrystals with the grain size 100 nm. The author of [22] developed a dislocation-kinetic approach, taking pile-up and annihilation of dislocations into account and regarding grain boundaries both as barriers to propagation of dislocations and as their sources and sinks. A simplified expression for the dependence of the yield strength on the strain magnitude and grain size is given by

$$\sigma_{\mathrm{y}}=f\alpha G\left(\frac{b}{L}\right)^{1/2}\left[\beta_0\exp\left(-fk\varepsilon\right)+\frac{\beta}{k}\left(1-\exp\left(-fk\varepsilon\right)\right)\right]^{1/2}, \tag{8}$$

where $f\sim 3$ (the Taylor factor for a polycrystal), k is the aggregate coefficient of dislocation annihilation depending on L, the strain rate, and the temperature, α is the dislocation–dislocation interaction coefficient, G is the shear modulus, b is the Burgers vector, β_0 is the parameter depending on the grain-boundary dislocation density, and β is the coefficient describing the pile-up of deformed dislocations. Evidently, for $fk\varepsilon\ll 1$ (i.e., when grains are relatively large), the yield stress depends on the grain size in accordance with the HP relation and $K_{\mathrm{y}}=f\alpha Gb^{1/2}(\beta_0+f\beta\varepsilon)^{1/2}$. For smaller grains ($fk\varepsilon\gg 1$), the dependence $\sigma_{\mathrm{y}}=f(L)$ is the inverse of relation (1), and it is easy to show that at the descending branch of the curve, $\sigma_{\mathrm{y}}\sim L$ or $\sigma_{\mathrm{y}}\sim L^{1/2}$, depending on which dislocation annihilation (single or pair) predominates at the boundaries.

Obtaining numerical results from (6)–(8) and comparing them with experimental data requires knowing many parameters and involves a number of assumptions. The calculated inflection points of the strength dependence of type (8), $\sigma_{\mathrm{y}}=f(L^{-1/2})$, are ~ 0.25 and ~ 0.3 nm$^{-1/2}$ for copper and nickel respectively [52], in excellent agreement with experiment (see Fig. 4). This approach was extended to the assessment of effects on the strength of dispersion [52] and bimodality [62] and to the analysis of the strain-rate sensitivity of the flow stress [84].

A detailed kinetic analysis of the behavior of dislocation pile-ups as barriers at intergrain boundaries in FCC nanometals (in the range $L=10-100$ nm, see Fig. 4) was made in [44]. Regarding the rate of change of the critical shear stress as a thermally activated process and assuming the relation of type (1) for τ, it is possible to derive expressions for the activation volume and the HP coefficient $K_{\mathrm{y}}^{\mathrm{II}}$. Table 2 contains theoretical and experimental data for several kinetic parameters.

The comparison shows fairly good agreement between the results (with the exception of shear rates for Ni). This means that the assumptions in [44] about the role of dislocation pile-ups in building up the strength of 'large' nanostructures are quite reasonable.

Various aspects of the physical mechanisms of deformed nanostructures have been summarized and analyzed in a series of publications [5, 8, 13, 34, 35, 85]. These mechanisms include the abnormal dependence of yield strength, plastic flow localization, rotational modes, the role of triple junctions, and heterogeneous and homogeneous nucleation of dislocations. For example, the authors of [34, 35], based on the energy approach for nickel and cubic silicon carbide,

Table 2. Comparison of theoretical and experimental values of the grain-boundary self-diffusion activation energy ΔH, the free volume v^*/b^3, and the shear rate $\dot{v}$ [44].

Metal	ΔH, eV		v^*/b^3		$\dot{v}$, s^{-1}	
	Experiment	Theory	Experiment	Theory	Experiment	Theory
Copper	0.64 – 1.08	0.70	1.1	1 – 10	1.3×10^5	1.1×10^5
Nickel	0.70 – 1.20	0.96	9.4	1 – 10	3.7×10^4	4.4×10^6

considered heterogeneous nucleation of dislocation loops at interfaces and homogeneous nucleation of full and partial dislocations under the effect of stress (1–7 GPa) inside nanograins undergoing deformation. It was shown that loop formation can be barrierless (athermal) if both the size of the emerging loop and the shear stress affecting it are sufficiently large. It is important that deformation processes in nanostructures of brittle high-melting-point metals and other compounds be considered together, notwithstanding the difference between them. The results of the studies in [34, 35, 85] give an idea of possible dislocation sources for intragrain deformation.

Other models used to analyze the deformation behavior of nanostructures with special reference to nonmonotonic strength changes (see reviews [15, 26] and monograph [8]) include a two-phase approach taking the relative increase in the 'soft' phase (interfaces and boundary regions), the diffusional creep along grain boundaries (Coble creep), and the diffusionless and activationless grain-boundary shuffling into account.

Computer experiments are of primary importance for understanding deformation mechanisms [9, 11, 19, 36, 77]; they definitively confirmed the existence of other sources, besides Frank–Reed's, of intragrain plastic shears. The known constraints of computer-assisted methods arising from idealization of the models and from the strain rates being used are self-critically discussed by the authors [see 11, 19].

As noted in Section 3.1, an agreement between theory and experiment requires a detailed analysis of the data representativeness, adequacy, and compatibility of the methods used to determine L. It was shown by the example of nanocrystalline copper [86] that the agreement between XRD and TEM findings exists only for objects with a narrow grain-size distribution and small average values (see also Table 1 [65]). Taken together, the aforesaid suggests numerous factors affecting the nanostructure strength and the necessity of accurate attestation of the objects of study by several independent methods when the aim of research is to examine size effects and identify characteristic points on dependences of the type $\sigma_y(\text{or}\, H) = f(L^{-1/2})$. Clearly, a comparison of the results reported by different authors, on the one hand, and theoretical and experimental data, on the other hand, needs comprehensive consideration, although this requirement is frequently disregarded.

As shown in [8, 27], each of the competing deformation mechanisms contributes to the overall effect in its own way, some playing a dominant and others a subordinate role, depending on the peculiar characteristics of a given nanostructure and deformation conditions. According to [27], the HP relation based on different dislocation models holds only for the critical size 10–30 nm, below which radical changes in the mechanical behavior occur due to the important contribution of deformation mechanisms associated with grain boundaries (shuffling, migration, dynamic recrystallization). Strict differentiation between the roles of each mechanism awaits further evaluation.

Brittle failure and crack propagation patterns in the framework of solid-state mechanics with respect to nanostructures have been analyzed in [14]. The authors draw attention to the role of nonequilibrium grain boundaries and their junctions in crack propagation. It is shown that an increase in the fracture energy owing to triple junctions may reach 20% for crystallites 10–20 nm in size.

As a rule, transcrystallite failure is unfeasible in nanomaterials because crystallites are much smaller than the Griffith crack nucleus; the critical length L_G of a crack can be found from the known expression

$$L_G \sim \frac{2E\gamma^*}{\pi\sigma_f^2}\,, \tag{9}$$

where E is the Young modulus, γ^* is the effective fracture energy, and σ_f is the tensile stress at the break. The choice of reasonable values for metals ($E = 100-200$ GPa, $\gamma^* \sim 10$ J m^{-2}, and $\sigma_f = 200-400$ MPa) and high-melting-point compounds ($E = 400-500$ GPa, $\gamma^* \sim 15$ J m^{-2}, and $\sigma_f = 400-600$ MPa) [87] gives the L_G value of the order of 10 μm.

Observation of fractures in nanoscale materials gives reason to suggest their intercrystallite nature [88]. Figure 10 depicts fractures in TiN samples illustrating intercrystallite crack propagation (a) and transformation of an intercrystallite fracture to an transcrystallite one with an increase in the grain size from 50 nm to 2 mcm (b). It roughly coincides with the above L_G estimate.

Disruption of nanoscale materials along grain boundaries is promoted by macro- and nanopores at interfaces that form during technological processing or arise in boundary regions under the effect of deformation. The latter source was

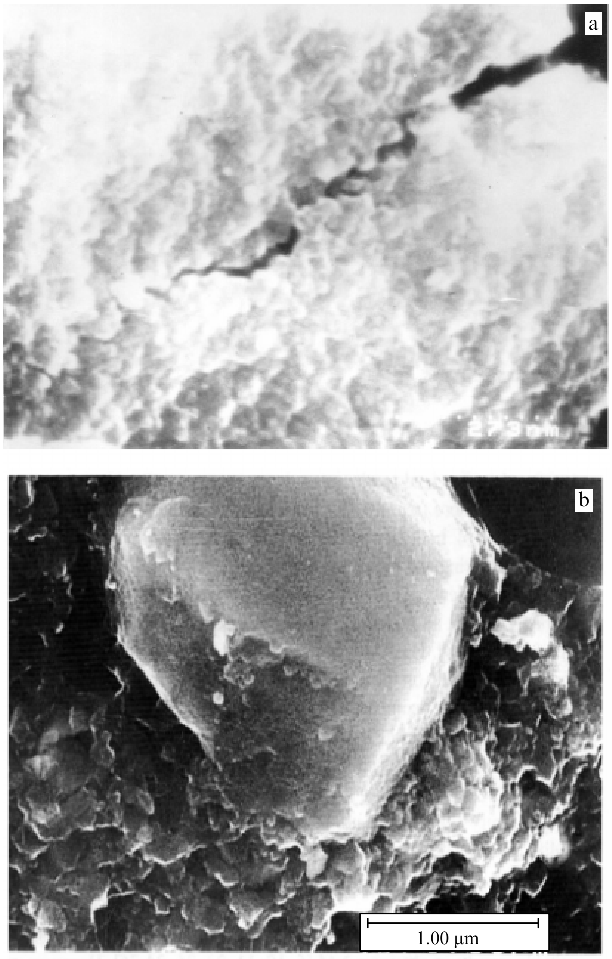

Figure 10. Fractures in samples of TiN nanopowder sintered at 4 GPa ($T = 1200\,^{\circ}\mathrm{C}$): (a) starting powder of ~ 18 nm particles, (b) starting powder of ~ 80 nm particles and isolated larger particles (~ 2 μm) [88].

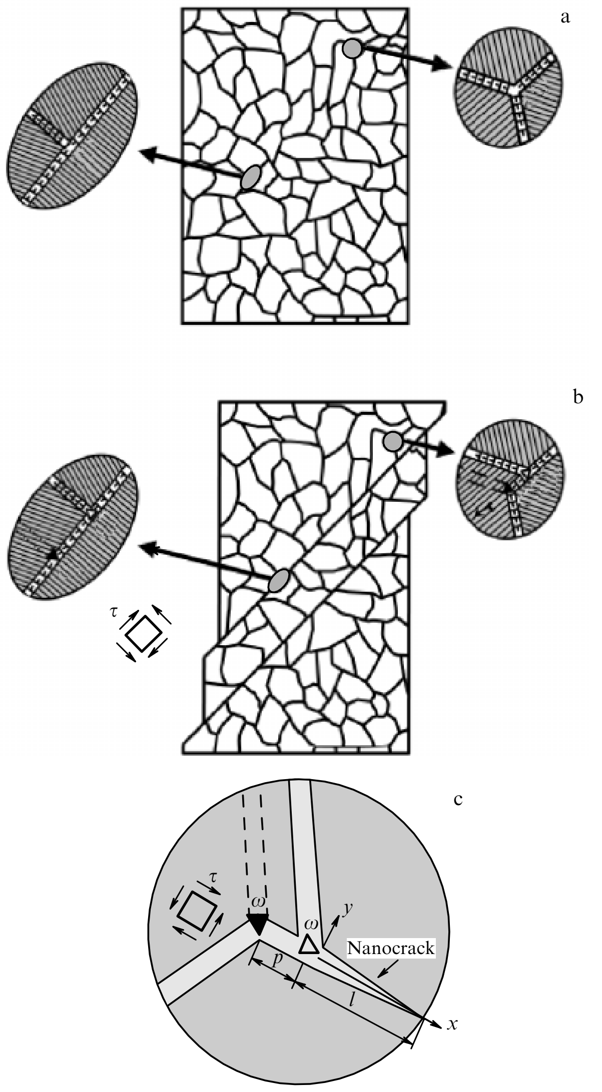

Figure 11. Formation of disclination dipoles for grain-boundary shuffling and emerging crack geometry: (a) initial state, (b) grain-boundary shuffling, (c) geometry of the emerging crack (τ, shear stress; $\pm\omega$, angular orientations of wedge disclination dipole; p, dipole arm; l, crack length) [89].

analyzed in [89] for corundum α-Al_2O_3 and cubic silicon carbide β-SiC. Figure 11 shows a putative scheme of formation of disclination dipoles during grain-boundary sliding and the geometry of an emerging nanocrack. The initial state (a) corresponds to two triple-juncture configurations, while situation (b) reflects grain-boundary shuffling that gives rise to disclination dipoles as a result of concurrent misorientations. In conjunction with local elastic stress, the dipoles can induce nanocracks. Parameter regions of their athermal nucleation are shown in Fig. 11c (ω is the angular orientation or strength of disclination and p is its arm). Specifically, no energy barrier is needed for nanocracks to form at 1 GPa, $\omega > 40°$, and $p > 2$.

The coalescence of nanocracks under the effect of uniaxial tensile stress in fragile nanoscale materials has been described in terms of the percolation theory [90]. It is shown that catastrophic failure occurs at a threshold critical stress slightly higher than that necessary for a nanocrack to form at a separate properly oriented intergrain boundary.

The knowledge of crack formation and behavior in nanoscale materials is important for understanding their cyclic and fatigue characteristics. Assessment of fatigue strength in nickel samples with the grain size 20–40 and 300 nm obtained by pulsed electrochemical deposition and in conventional macrocrystalline Ni ($L = 10$ μm) showed that a decrease in the grain size leads to an enhanced breaking stress over the entire cycle range (up to 10^7 cycles at 10 Hz), even though the difference between $L \sim 30$ and ~ 300 nm (much greater values than for ordinary Ni) was insignificant [91]. Cracks in the treated nanosamples were much longer and developed faster than in conventional Ni. Similar results were obtained in dynamic tests using an Al–7.4% Mg alloy ($L = 300$ nm) fabricated by low-temperature milling with subsequent consolidation. This means that the fatigue strength of nanoscale materials decreases due to the more active crack development and fusion. The results of cyclic deformation of copper samples obtained by the MPD technique are presented in greater detail in monograph [12], where the marked effect of preliminary annealing is documented along with higher saturation stress in nanomaterials, compared with their macrocrystalline analogs; the Bauschinger effect that reflects the increased dislocation density during cyclic strengthening is also more pronounced in the former entities.

It is worth mentioning that examination of indentation imprint surfaces in nanostructured films by HRTEM revealed two types of deformation, heterogeneous with stepped shear bands (in TiB_2, Fig. 12a, b) and homogeneous (in NiN, Fig. 12c, d) [33, 88]. In the former case, the shears are localized in the direction of indentation, with the step height and width varying from ~ 100 to hundreds of nanometers. As the indentation load increases (from 1 to 5 H), the imprints in TiN show cracks (Fig. 12d), while steps are absent. It may be conjectured that homogeneous deformation is associated with the columnar structure inherent in TiN films, i.e., with the sliding of the columns against each other (Fig. 9). Simultaneous homogeneous and heterogeneous deformation is typical of amorphous alloys [92], which gives cause to suggest similarity between mechanisms of plastic deformation in amorphous and nanocrystalline materials.

In conclusion, it is appropriate to consider the dispergation limit $L_{\min}$ with reference to deformation. Apart from the theoretical interest, this issue is important for the practical purpose of using high-temperature milling and MPD techniques to manufacture nanoparticles and bulk nanomaterials with minimally small crystallites. This problem was addressed in many works (see, e.g., [93–97]). It is obvious from general considerations that each object (metal, alloy, or compound) has a characteristic $L_{\min}$ value depending on its physical, mechanical, and chemical properties. Reference [93] summarizes experimental $L_{\min}$ values for metal particles (normalized to the Burgers vector) in relation to the melting temperature, hardness, milling temperature, self-diffusion activation energy, volume elasticity modulus, and stacking fault energy. These data provided a basis for calculation of $L_{\min}$ in the case of limiting dispergation under the assumption of equal rates of the competing strengthening (generation of dislocations) and recovery (annihilation and recombination of dislocation) processes. The estimated $L_{\min}$ values ranged from 6–7 nm (Ir, Rh, Pd, W) to 25 nm (Al, Ag).

The results of milling tungsten carbide in [96] were used to develop (in the framework of the dislocation concept) a kinetic dispergation model with the consumption of milling

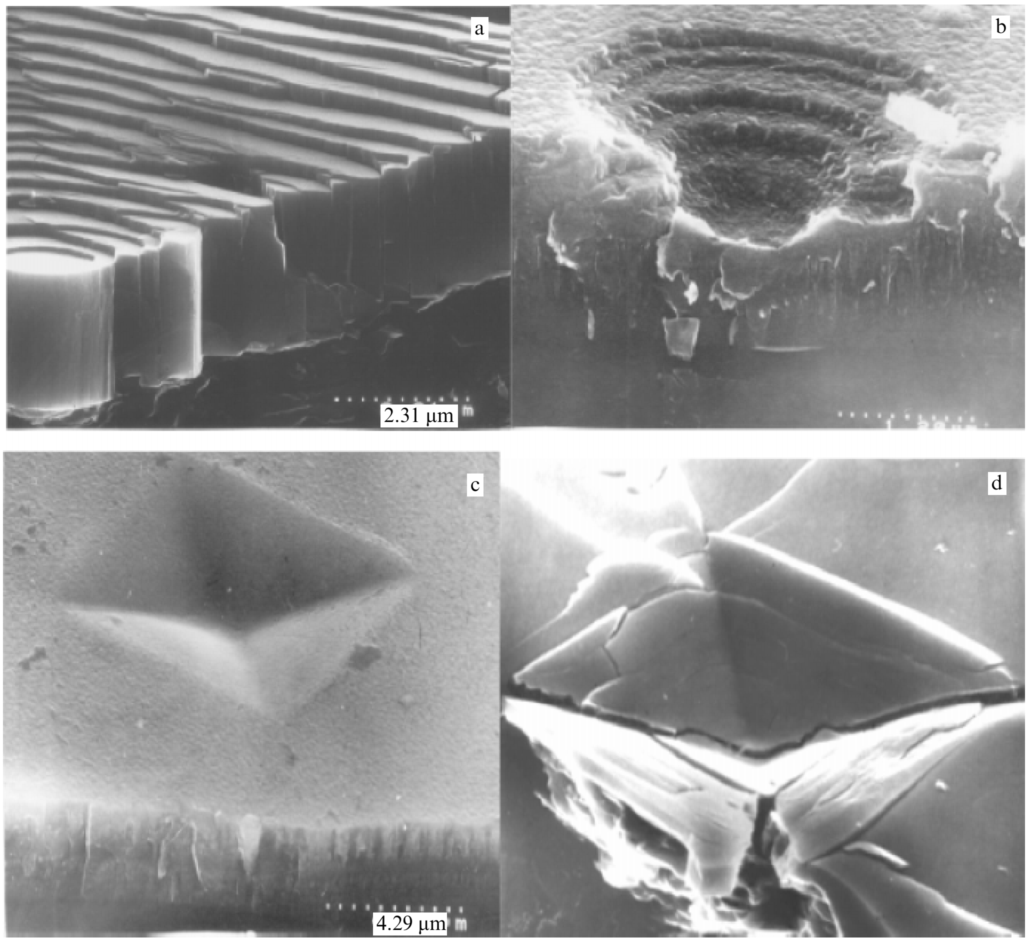

Figure 12. Indentation imprint surface in TiB_2 (a, b) and TiN (c, d) films [33, 88].

energy taken into account not only for the formation of new surfaces but also for the creation of new microstresses. The authors maintain that their experimental data on the WC milling kinetics up to the size of coherent scattering regions, $\sim$ 10 nm ($t \sim 15$ hr), are in excellent agreement with the theoretical curve. However, the method used for its calculation is far from being explicit.

Dispergation limits were considered in [94, 95, 97] for MPD by ECAP. Analysis of a model simulating the formation of low-angle boundaries due to relaxation of juncture disclinations showed that the minimally attainable grain size does not exceed 100 nm [95]. Junction disclinations were also used in [94], but these authors additionally took accommodation through grain-boundary diffusion into account, which enabled them to evaluate the temperature dependence of the dispergation limit for certain metals and Al or Mg-based alloys. They concluded that the minimal grain size ($\sim$ 300 nm or greater) is determined by diffusional accommodation of juncture dislocations and obtained good agreement between its experimental and theoretical values at the deformation temperatures 100 – 400 °C. The model in [97] predicts that dispergation during cold deformation depends not only on the amount of accumulated strain but also on the contribution of the dislocation and disclination mechanisms determining intra- and interfragmentary components of the total deformation.

A preliminary analysis of the results in [93–97] shows that all the authors reported good agreement between theory and experiment, although they proceeded from different assumptions. Because the representativeness of experimental findings (grain size distribution, methods of its evaluation, etc.) is not specified, their conclusions can be accepted only with some reservations. In this context, Ref. [98] is of special interest because MPD treatment of annealed copper samples with the initial grain size 100–250 μm was there performed by dynamic compression at the temperature of liquid nitrogen and included detailed attestation. The deformation resulted in a matrix structure of fragmented nanograins and twins. It was shown using MPD and HRTEM that a 2.1% deformation produced fragmented grains 120–160 nm in length and 45–120 nm in diameter, while twins with $\sim$ 47 nm thick lamellae occupied 33% of the total volume. The mean grain size was 68 nm, the yield strength amounted to 633 PMa, the elongation until disrupture was 11%. Both the strength and the ductility of these samples were somewhat lower than in samples with a purely twining structure studied by the same authors [41–43] (see Fig. 4 [43]). On the other hand, they exemplified bulk nanomaterials rather than electrolyte layers (the thickness 12 mm and the diameter 9 mm). More detailed studies of their mechanical properties are underway [98].

Conditions for the formation of nanostructured entities during MPD were considered at length in [99, 100]. Three possible scenarios were postulated (Fig. 13). When the conditions favor rearrangement of dislocations and disclinations (e.g., in pure metals), plastic deformation is followed by low-temperature dynamic recrystallization. Local regions of

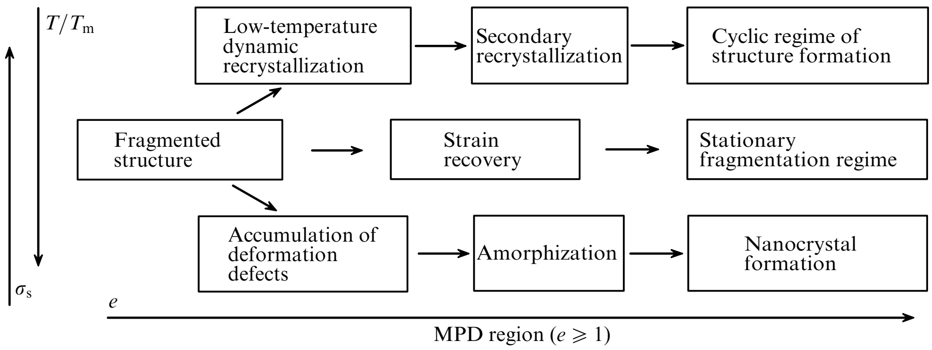

Figure 13. Main scenarios for the development of structural processes during MPD [99]; e is the actual deformation.

the structure 'eliminate' deformation defects, and the newly recrystallized grains again begin to accumulate dislocations and other defects. When the mobility of plastic flow carriers is relatively low (e.g., in intermetallics), MPD promotes phase transformations (usually of the 'crystal-to-amorphous phase' type) (see Fig. 13). An intermediate situation is feasible in which disclination rearrangements (such as described in [35, 85]) serve as an efficacious elastic energy dissipation channel and lead to the formation of a relatively stable fragmented structure at the stage of transition from the ordinary deformation to MPD [101]. Evidently, the transition from one structurization scenario to another depends on the deformation temperature. The proposed approach suggests at least two implicit phenomena in the case of MPD [102]. One is the low-temperature dynamic recrystallization and amorphization ($T < 0.4T_m$) and the other is a cyclic structure formation during MPD. Both variants are fairly well substantiated by theoretical and experimental data [102].

To summarize consideration of MPD-associated processes, it is appropriate to mention one more interesting phenomenon, the nanoscale crystallization in amorphous alloys during low-temperature deformation in a Bridgeman chamber. Formation of nanocrystals during MPD at room temperature has been described by many authors [103–105]. Nanocrystals 30 nm or less in size spread uniformly over the entire volume of the amorphous matrix. It is noteworthy that they 'survived' after a huge plastic deformation and formed after MPD at room and cryogenic (77 K) temperatures [105].

4. Other mechanical properties

4.1 Elastic properties. Nanoindentation. Fracture toughness

It was shown using nanostructured samples of Ni–2 mass % P ($L = 4-29$ nm) [37] and ZrO_2-3 mass˜% Y_2O_3 ($L = 23-130$ nm) [106] that the Young modulus decreases appreciably starting from the respective grain size ~ 30 and ~ 55 nm, (Fig. 14). Differentiation between the effects of the grain boundaries and triple junctions in [37] based on additive considerations and data in Fig. 2 allowed obtaining elastic characteristics for grain boundaries ($E_{gb} = 184$ GPa) and triple junctions ($E_{tj} = 143$ GPa); the value of E for the grain body (204 GPa) was close to that for macrocrystalline Ni (207 GPa). The lower values of E_{gb} and E_{tj} were attributable to the increased free volume and interatomic distances at the interfaces.

Molecular dynamics calculations for iron with the grain size 6, 9, and 12 nm revealed a decrease in the Young modulus by 0.7–0.8 from the value typical of macrocrystalline iron [107], in agreement with some experimental data. Many experimental studies disregarded the effect of porosity on the elastic properties of nanoscale materials. The results in [37] and [106] are quite reliable in this respect because, on the one hand, they are obtained by the ultrasound method with due corrections for the role of porosity and phase composition [106], and on the other hand, the indentation technique was used, whose results are virtually independent of porosity [37].

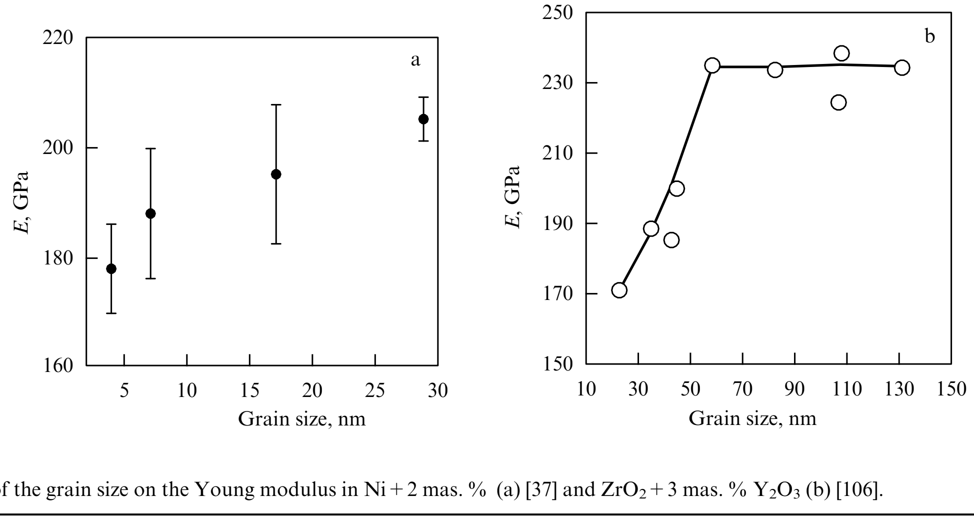

Figure 14. Effect of the grain size on the Young modulus in Ni + 2 mas. % (a) [37] and $ZrO_2 + 3$ mas. % Y_2O_3 (b) [106].

As work on the synthesis of nanowires and nanotubes gains momentum, the elastic properties of these objects are being studied on an increasingly larger scale. The Young modulus for gold wires in the diameter range from 40 to 250 nm shows no size dependence and equals 70 ± 11 GPa, i.e., approximates the tabulated value for Au, $E = 78$ GPa [108]. At the same time, the respective yield strength for diameters 200 and 40 nm is 3.5 ± 1.1 and 5.6 ± 1.4 GPa, (the latter value is close to the theoretical strength $E/10$), or much greater than 55–200 MPa, typical of macrocrystalline gold. We also note that the deformation is associated with considerable strengthening; in other words, the dislocation activity is observable within the entire size range being studied.

The methods for the measurement of the Young modulus in nanoscale objects are complicated, and the values obtained are sometimes ambiguous. Different authors report contradictory data for ZnO wires. According to [109], E increases appreciably with decreasing the size starting from the diameter 120 nm, while other estimates [110] and certain experimental findings suggest an inverse relation, i.e., a decrease in E after the diameter reduction to below ~ 80 nm. This issue awaits a more detailed study for the choice of a better specified measuring technique and its theoretical substantiation. Subtleties that occur in measuring eigenfrequencies of nanostructured objects during evaluation of their hardness characteristics are discussed in [111].

Nanoindentation is now commonly used to measure hardness and the elastic properties of films and surface layers. This method is described at greater length in [112]. Figure 15 presents a general loading–unloading scheme and the parameters studied, i.e., hardness $H = P_{\max}/B$, $S = \mathrm{d}P/\mathrm{d}h$, the Young modulus of the film-indenter system (effective modulus) $E^* = S/2(\pi/B)^{0.5}$, and the so-called elastic recovery $R = (h_{\max} - h_{\mathrm{f}})/h_{\max}$; here, B is the imprint projection area depending on the maximum indentation depth $h_{\max}$ and h_{f} is the residual imprint depth (after unloading). The elasticity modulus of the film, E_{film}, is in turn given by the relation

$$\frac{1}{E^*} = \frac{1 - \nu_{\mathrm{ind}}^2}{E_{\mathrm{ind}}} + \frac{1 - \nu_{\mathrm{film}}^2}{E_{\mathrm{film}}}\,,$$

where ν_{ind} and ν_{film} are Poisson coefficients of the intender and the film, and E_{ind} is the indenter elasticity modulus. It should be borne in mind, however, that the results of such measurements depend on the choice of the optimal load and the surface properties of the object. Figure 16 illustrates the dependence of deformation characteristics for two nitride-boride films, one with the hexagonal structure I ($(\mathrm{Ti}(\mathrm{B}_{0.73}\mathrm{N}_{0.2}\mathrm{O}_{0.05}\mathrm{C}_{0.02})_{1.56}$, $L = 4-8$ nm, thickness 1.7–1.8 μm) and the other with the cubic structure II ($\mathrm{Ti}(\mathrm{N}_{0.49}\mathrm{B}_{0.34}\mathrm{O}_{0.12}\mathrm{C}_{0.05})_{1.49}$; $L = 3-6$ nm, thickness 1.2–1.3 μmm) [113]. Evidently, H values are unrelated to P only for the hardness in the small load range ($P = 5-30$ mH), which reflects the effect of stress load known from durometry. The values of E and R in the studied load range continue to increase. Notably, these films are very similar in terms of elastic recovery, i.e., a fairly provisional brittleness parameter ($R = 0$ is the total plasticity, $R = 1$ is the total elastic recovery), but their H and E values are substantially different.

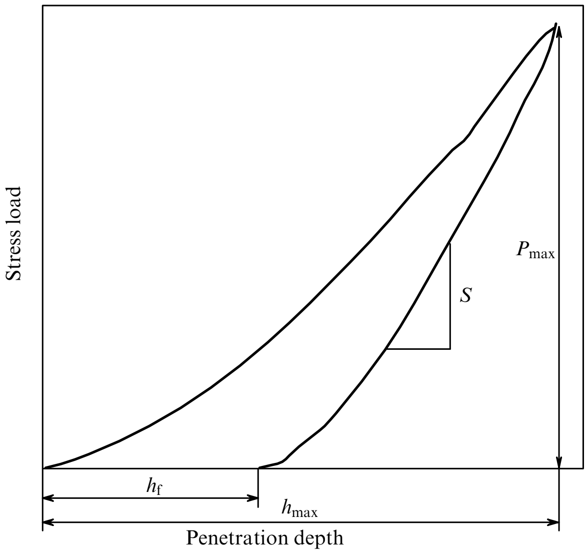

Figure 15. Plots of the indentation depth versus stress during loading and unloading.

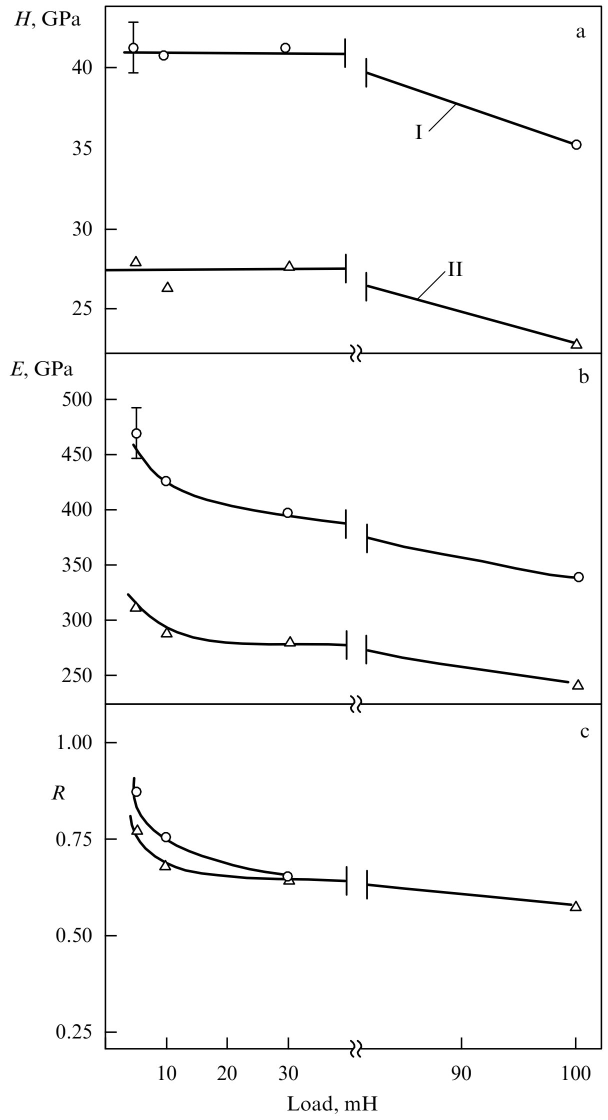

Figure 16. Effect of maximum load on the hardness (a), the Young modulus (b), and the elastic recovery (c) for I (○) and II (△) films [113].

It is interesting to compare these values with experimental results obtained by other methods. For films I and II, $E_{\mathrm{I}} = 460 \pm 50$ GPa, $H_{\mathrm{I}} \sim 49$ GPa, $E_{\mathrm{II}} = 480 \pm 100$ GPa,

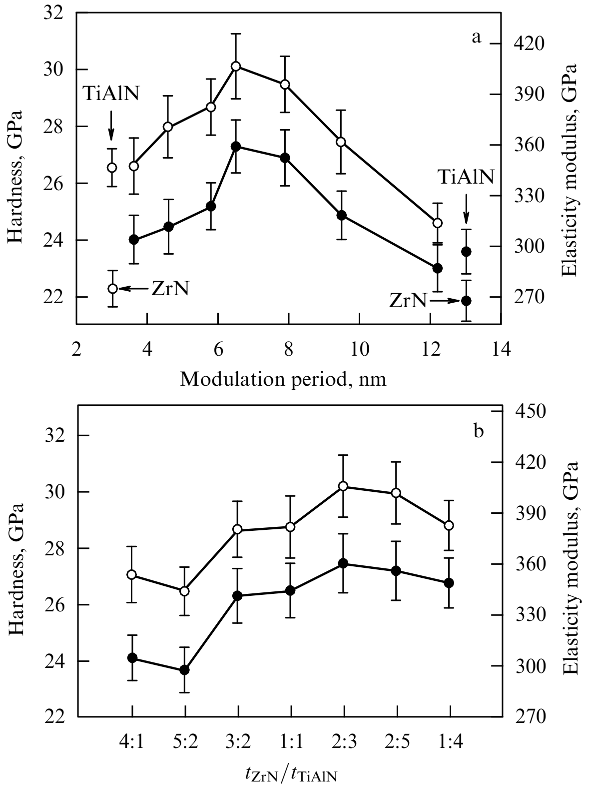

Figure 17. Plots of the hardness (○) and the Young modulus (●) in multilayer ZrN/(TiAl)N films versus the modulation period Λ (a) and the thickness ratio (b) [119].

and $H_{\mathrm{II}} \sim 49$ GPa. Taken together, these data and those in Fig. 16 indicate that the results of H and E measurements by different methods are comparable only for film I; the indentation method yields smaller values for film II. The causes of this difference (including surface roughness) are discussed at greater length in [113, 115]. Here, it is important to note that the comparison of hardness and elasticity data from various authors requires a thorough discussion of experimental conditions. In this context, the use of the H^3/E^2 criterion for the evaluation and prediction of the resistance of nanostructured films to plastic deformation (see, e.g., [81, 116–118]) appears to be of little promise.[4]

For all that, the nanoindentation technique may be useful to optimize manufacturing regimes of nanomaterials and monitor their deformation despite somewhat ambiguous absolute measurement data. Figure 17 shows variations in the hardness and the Young modulus in multilayer ZrN/(TiAl)N films depending on the modulation period (the total thickness of individual layers $\Lambda = t_{\mathrm{ZrN}} + t_{\mathrm{(TiAl)N}}$ and $t_{\mathrm{ZrN}}/t_{\mathrm{(TiAl)N}}$ ratio) [119]. Clearly, H and E undergo nonmonotonic changes, reaching respective maxima ~ 30 and ~ 360 GPa at $\Lambda = 6$ and $t_{\mathrm{ZrN}}/t_{\mathrm{(TiAl)N}} = 2{:}3$. Films with such characteristics have the layered texture {111}, a low residual compressive stress, and a high scratching (failure) resistance. Moreover, the absolute E and H values for the starting ZrN and (TiAl)N films (Fig. 17) differ from those reported by other authors (see [29]); this confirms the above considerations about nanoindentation.

Some authors, based on the results of experiments with thin SnO$_2$, (In,Sn)O$_2$, TiO$_x$N$_{1-x}$ films, suggested using the nanoindentation technique for measuring the fracture toughness (cracking resistance) K_{IC} [120–122]. For example, the values of hardness, the Young modulus, and K_{IC} derived from strain diagrams for oxide-nitride films proved to be 9 GPa, 117 GPa, and 1.8 ± 0.2 MPa m$^{1/2}$, respectively [121]. For carbon carbide (CN$_x$) films, a reasonable K_{IC} value 5.8–6.2 MPa m$^{1/2}$ close to that for diamond (5–6 Mpa) was reported [122].

A markedly enhanced fracture toughness was demonstrated by the indentation technique in an iron-based amorphous alloy containing the optimal amount of the nanocrystalline phase [123].

Other methods, besides nanoindentation, can be used to measure fracture toughness in nanoscale films; a challenging problem of today is to standardize them as regards the optimal choice of substrate, load, strain rate, etc. [120].

Data on the fracture toughness of nanocomposites comprising high-melting-point compounds are summarized in several reviews [124, 125]. Analysis of Table 3 shows that a substantial increase in K_{IC} occurs only in MgO and Al$_2$O$_3$-

Table 3. Hardness and fracture toughness of TiN, WC, and Al$_2$O$_3$ nanocomposites (σ_{f} is the failure resistance).

Composite; reference	Relative density, %	Grain size, nm	Hardness, GPa (load, H)	K_{IC}, MPa m$^{1/2}$
TiB$_2$/TiN [125] (25–75 %)	97–99	TiB$_2$(400); TiN(80)	26–32 (0.5)	4.7–5.2
TiN [125]	98	80	23 (0.5)	3.8 ± 1.8
WC/18MgO [126]	99.2	< 50	15 (500)	14
WC [126]	99.3	~ 25	23 (500)	4
WC/32Al$_2$O$_3$ [127]	99.2	< 50	16 (500)	15
WC/6ZrO$_2$ [128]	~ 100	WC(350); ZrO$_2$(100)	23–24 (100)	~ 6
WC/6Co [128]	~ 100	Conventional	~ 17 (100)	~ 14
Al$_2$O$_3$ [124]	—	$\sim 2 \times 10^2$	$\sigma_{\mathrm{f}} = 462$ MPa	3.7
Al$_2$O$_3$/5Ni [124]	—	—	$\sigma_{\mathrm{f}} = 462$ MPa	4
Al$_2$O$_3$/3SiC [124]	—	—	$\sigma_{\mathrm{f}} = 760$ MPa	5.05
Al$_2$O$_3$ [129]	99.2	$\sim 5 \times 10^3$	17.5 (500)	3.25
Al$_2$O$_3$/5SiC [129]	97.7	Al$_2$O$_3$(3.5×10^3); SiC(12)	17.8 (500)	3
Al$_2$O$_3$/5SiC [129]	98.4	Al$_2$O$_3$(4×10^3); SiC(55)	18.3 (500)	2.75
Al$_2$O$_3$/5SiC [129]	98	Al$_2$O$_3$(2×10^3); SiC(90)	18.5 (500)	3.05
Al$_2$O$_3$/5SiC [129]	99	Al$_2$O$_3$(3.5×10^3); SiC(115)	18.8 (500)	3.45
α-Al$_2$O$_3$ [130]	99.8	349 ± 10	—	3.30 ± 0.14
Al$_2$O$_3$/7.5BaTiO$_3$ [130]	99.6	256 ± 13	—	5.36 ± 0.38
Al$_2$O$_3$/15BaTiO$_3$ [130]	99.9	326 ± 18	—	4.34 ± 0.39

---

[4] This criterion is poorly based physically, and its numerical values may contain serious measuring error.

doped WC composites with a concomitant decrease in hardness. The cause of such behavior remains to be clarified. Changes in K_{IC} in other objects are less significant. The main factors playing a role in the possible change in the hardness and fracture toughness variation in ceramic nanocomposites are the stressed state, changes in the critical crack length, the dislocation activity, the grain-boundary strengthening, and the strengthening by nanoinclusions (for an Al_2O_3-SiC system, see [124, 131]).

Kinetic studies of the decomposition of standard nano- and macrocrystalline nickel demonstrated an enhanced strength and a small increase in the cracking resistance of nanostructures associated with the reduced plasticity and impact viscosity; the relatively low cracking resistance was due to inhomogeneities in the nanostructured material [132].

4.2 The temperature effect. Creep and superplasticity

Evaluation of the low-temperature strength of nanocrystalline Cu, Ni, Nb, Ti, and Al samples prepared by ECAP (grain size 50–500 nm) showed that the temperature dependence (from 4.2 to 290 K) of the yield strength can be arbitrarily divided into a few sections as follows: a weak temperature dependence in the low-temperature range (with an increase in σ_y followed by a decrease in the case of Ti), a greater decrease in σ_y, and finally a smoother dependence $\sigma_y = f(T)$ [133, 134]. The length of these sections is different for different metals. Strain strengthening predominates for copper at low temperatures; the yield strength of nanocrystalline samples depends on the type of deformation.

Nanostructured films based on high-melting-point compounds like TiN, TiB_2, and Si_3N_4 have a stable structure and hardness up to the annealing temperatures 1000–1200 °C. The hardness of TiN–ZrN and TiN–AlN systems increases with the temperature due to the strengthening effect of the nanoparticles released during spinodal decomposition (Fig. 18) [48, 135–138].

As noted above (Section 3.2), the temperature of the ductile–brittle transition in SiC nanowires and other fragile nanoscale objects is very low. The low temperature of the transition to a plastic state, an enhanced creep rate $\dot{\varepsilon}$, and the early manifestation of superplasticity in nanomaterials are conditioned by the abundance of interfaces and their mobility. Figure 19 presents strain diagrams of nanocrystalline Ni and MgO samples [139, 140]. They clearly show changes in the mechanical behavior of both materials, as well as the transition from restricted plasticity (for Ni at

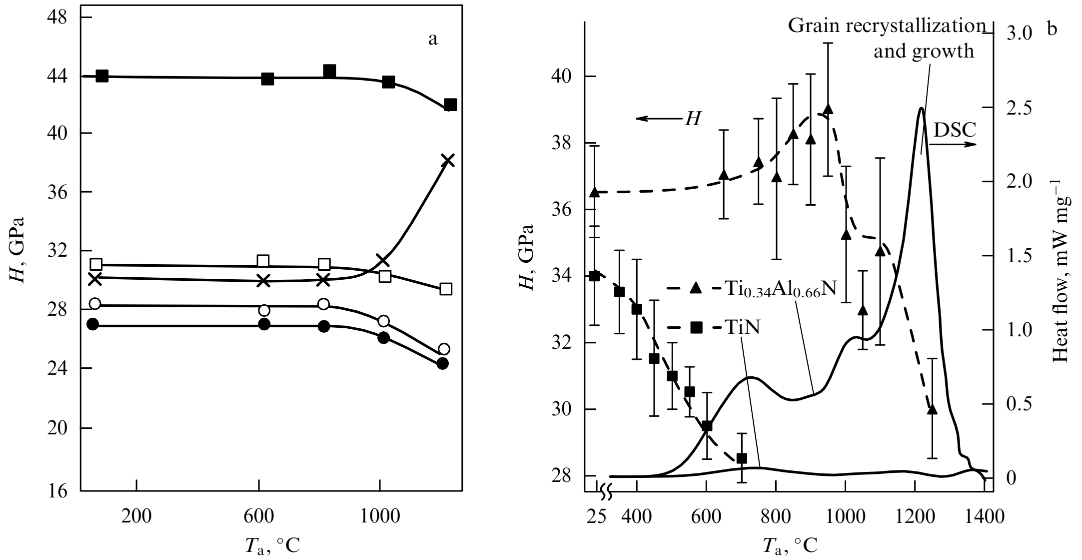

Figure 18. Effect of the annealing temperature on the hardness of nanostructured films: (a) ■, TiN/ZrN (20 layers); □, TiN/ZrN (10 layers); ×, (TiZr)N; ○, TiN; ●, ZrN [135]; (b) ▲, (TiAl)N; ■, TiN [136]. DSC is the data obtained with a differential scanning calorimeter.

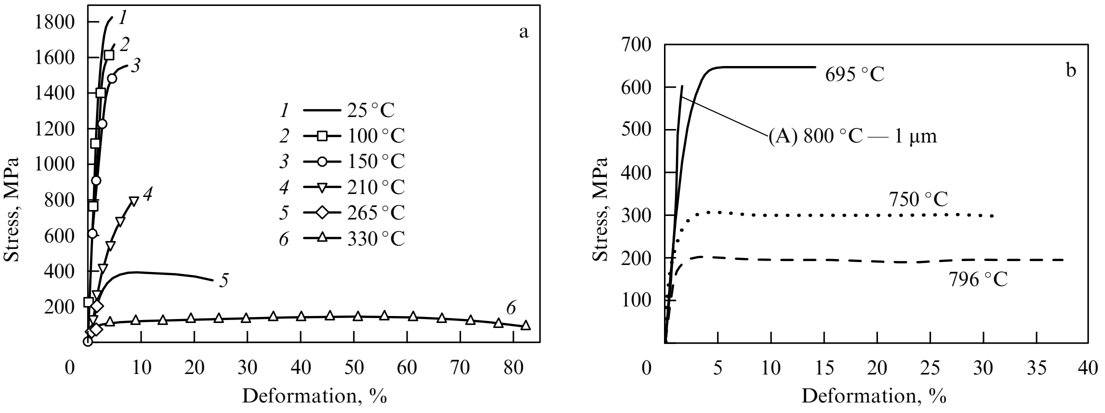

Figure 19. Strain diagrams of nano-Ni (a) and nano-MgO (b) at different temperatures; curve A shows the deformation of MgO with the grain size ~ 1 μm [139, 140].

$T < 200\,^\circ$C) or virtually absent plasticity (for macrocrystalline MgO at $800\,^\circ$C) to its well-apparent manifestations. The strain-rate sensitivity exponent m for crystalline Ni at the test temperatures 25 and $330\,^\circ$C is 0.02 and 0.3–0.4, respectively. The sulfur segregation and formation of low-melting-point sulfides at intergrain boundaries are supposed to promote intergrain sliding.

The mechanisms of high-temperature strain and creep in nanoscale materials are discussed in many publications [10, 15, 20, 140–145]. The expression for the creep rate is usually written in the form

$$\dot{\varepsilon} = A\,\frac{Gb}{kT}\left(\frac{b}{L}\right)^p\left(\frac{\sigma}{G}\right)^n\left(D_{\mathrm{v}} + \pi\xi\,\frac{D_{\mathrm{gb}}}{L}\right), \tag{10}$$

where A is a numerical coefficient, D_{v} and D_{gb} are the bulk and boundary diffusion coefficients, b is the Burgers vector, ξ is the boundary width, and p and n are the exponents in the dependences $\dot{\varepsilon} \sim (1/L)^p$ and $\dot{\varepsilon} \sim \sigma^n$ (n is the inverse of the strain-rate sensitivity exponent of the flow stress m, $n = 1/m$). The dislocation creep is realized at $p = 0$ and $n > 3$; grain-boundary (Coble's) sliding ($p = 3$, $n = 1$), diffusional (Nabarro–Herring's) creep ($p = 2$, $n = 1$), and other combined mechanisms occur at $p \geqslant 1$ and $n \leqslant 3$. Also considered are the contribution of the boundary diffusion and the diffusional flow along triple junctions, whose number increases substantially starting from the grain size $\leqslant 10$ nm (see Fig. 2 above). The modified expression for the creep rate with the account of the triple-junction diffusion coefficient D_{tj} has the form

$$\dot{\varepsilon} = \frac{A_{\mathrm{tj}} D_{\mathrm{tj}} \Omega \xi^2 \sigma}{kTL^4}, \tag{11}$$

where Ω is the atomic volume [146].

An analysis of experimental nanocrystal creep data reveals a rather wide range of observed n values. For example, for nanocrystalline Ni, $n = 1, 2, 5$ ($T = 25\,^\circ$C, $L = 6, 20, 40$ nm); $n = 1, 6$ ($T = 25, 100\,^\circ$C, $L = 30$ nm); $n = 8, 10, 12$ ($T = 100\,^\circ$C, $L = 40$ nm) [15, 143–145]. Although these differences are to a certain extent due to dissimilar experimental conditions (stress interval, strain rate, nonstationary creep duration, grain growth, etc.), they reflect the complex character of the mechanism ensuring the deformation not only by grain-boundary processes (evidenced by a low activation energy) but also through dislocation contribution. Operation of the Nabarro–Herring–Coble mechanism was confirmed in a computer experiment with nano-Pd ($L = 3.8-15.2$ nm, $T = 900-1300$ K), which demonstrated a linear stress dependence of $\dot{\varepsilon}$ and the transition from $p = 3$ at L to $p = 2$ (i.e., to a purely diffusional creep) at the grain size below 7 nm [141]. Activation energies of bulk and boundary self-diffusion in Ni are ~ 280 and ~ 60 kJ mol^{-1}, respectively, which suggests a substantial contribution of grain-boundary processes to the nanostructure deformation at high temperatures [20].

The role of diffusibility in deformation processes is equally important in the case of superplasticity, i.e., at high deformation characteristics (hundreds of percent or more) at the temperatures at least $\sim 0.5T_{\mathrm{m}}$ and the strain rate around 10^{-4} s^{-1}. It is the so-called 'structural' superplasticity that is observed at the grain size less than 10 μm. However, the small grain size itself is insufficient for superplasticity to manifest itself. It needs shears along the grain boundaries and their accommodation in triple junctions depending on the diffusibility at interfaces [20, 147, 148].

Comparison of different contributions to the grain-boundary strain rate in [148] showed a nonmonotonic variation in this characteristic depending on the grain size; it increases substantially in the nanometric range with a maximum at $L \sim 10^4 b$ (i.e., at the level of 2–3 μm) in agreement with the values for certain alloys.

Many authors [18, 20, 21, 149–158] reported studies on the superplasticity of nanoscale materials (metals, alloys, intermetallides, high-melting-point compounds) prompted by the possibility of decreasing the temperature of this process for practical purposes. Some of their results are presented in Table 4.

Table 4. Superplasticity characteristics of selected nanoscale materials.

Object; reference	Grain size, nm	Temperature, °C	Stress, MPa	n, q ($\dot{\varepsilon} \sim \sigma^{\mathrm{n}}/L^{\mathrm{q}}$)	Maximum strain, %	Strain rate, s^{-1}
Ni [149]	20	350	~ 400	—	300	1×10^{-3}
Al-1420* [149]	100	250	150	—	350	1×10^{-1}
Al-1420 [21]	700 – 800	400	—	—	1620	1×10^{-2}
Ni_3Al [149]	50	650	1500	—	375	1×10^{-3}
$ZrO_2(3Y) + Al_2O_3 + MgAl_2O_4$ [152]	~ 100	1300 – 1450	10 – 100	$n \sim 2$	—	$10^{-4} - 10^{-2}$
Ni-22.6%Co [153]	20	500	—	$n = 2$	279	5×10^{-3}
Ni [153]	65	450	—	$n = 2$	550	2×10^{-3}
$Si_3N_4(2\%Al_2O_3 + 5\%Y_2O_3)$ [154]	68	1450 – 1600	100 – 400	$n = 2, q \sim 1$ $n = 1, q \sim 3$	50	$10^{-5} - 10^{-3}$
Al-7034** [155]	300	400	~ 10	$n = 2$	1090	10^{-2}
Mg-ZK60*** [155]	800	200		—	1310	2×10^{-4}
$ZrO_2(3Y) + 30\%Al_2O_3 + 30\%MgAl_2O_4$ [156]	280 – 450	1500 – 1650	—	—	390 – 2500	$10^{-2} - 1$
Ti – 6%Al – 4%V [157]	100 – 600	500 – 800	—	—	360 – 516	10^{-2}

* Al – 5.5%Mg – 2.2%Li – 0.12%Zr;
** Al – 11.5%Zn – 2.5%Mg – 0.9% Cu – 0.2%Zr;
*** Mg – 5.5%Zn – 0.5%Zr.

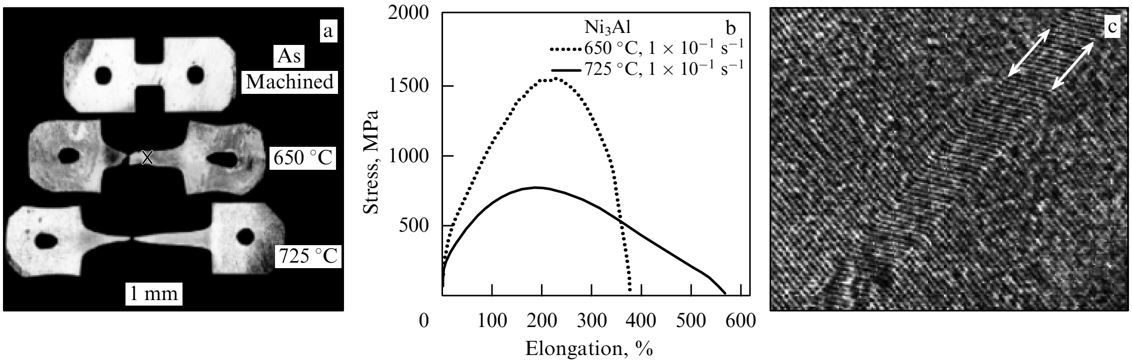

Figure 20. General view of nanocrystalline Ni_3Al samples before and after trial (a); strain diagram (b); a high-resolution (×7500000) electron micrograph (c) of the portion marked by X in Fig. 20a [150, 157].

The data in Table 4 suggest that the temperature at which superplasticity manifests itself in Al, Ti, Mg, and Ni-based alloys and in a three-phase oxide composition can be reduced owing to the nanostructure; simultaneously, the strain rate increases to values characteristic of the so-called high-strain-rate superplasticity. The practically acceptable strain rates are $\geqslant 10^{-2}$ s^{-1} at low temperatures and flow stress given a homogeneous-type deformation without neck formation and cavitation phenomena (development of pores and cavities). Some results presented in Table 4 deserve special attention. Specifically, the superplasticity of oxides and silicon nitrides occurs at high temperatures. The data for metals and alloys refer to stretching tension conditions, whereas the results in [152, 154, 156] were obtained for compression, i.e., under milder stress conditions. Moreover, the dynamic recrystallization accompanying superplastic treatment and leading to an increase in the starting grain naturally impairs parameters of superplasticity. For example, the deformation of Ni–Co nanoalloys and nanocrystalline Ni in [153] promoted grain growth up to 1–2 μm. Intense recrystallization of Ni samples was observed in [149], although structural changes in an Al nanoalloy were less pronounced, and the structure of Ni_3Al remained unaltered at the testing temperature 650 °C.

The mechanisms of recrystallization in general and of dynamic recrystallization in nanoalloys during superplastic treatment in particular are discussed at great length in monographs [159, 160]. The authors emphasize the role of the grain boundary state in intergrain shuffling and manifestations of superplasticity that affect the nonmonotonic temperature dependence of superplasticity [148, 160].

The authors of [149] noticed one more complication (enhancement of the flow stress with decreasing the temperature) that should be taken into consideration in the development of superplastic materials. For example, the superplasticity temperature in nanocrystalline Ni_3Al was about 400° lower than in a microcrystalline sample, while the flow stress was as high as 1.5 GPa (Fig. 20b). Evidently, many characteristics presented in Table 4 need to be further improved by choosing the optimal nanostructure and treatment conditions.

Figure 20 presents the general view of Ni_3Al samples before and after testing, along with their strain diagram and electron micrograph of the intergrain boundary [150, 157]. Also, the figure shows an appreciable strain strengthening and a marked temperature dependence of the flow stress associated with the transition from the essentially elongation at 650 °C to neck formation and the nonuniform elongation until disruption at 725 °C. A characteristic feature of the thin foil prepared for HRTEM from the sample portion marked by X is the twin boundary structure and the absence of dislocations inside the grains, whose shape did not change after deformation. The lack of high dislocation activity was also documented for other (Al and Zn) superplastic nanoscale alloys. The main deformation mechanism is assumed to be grain-boundary shuffling [21]. Dislocations and twins in deformed Ni and Ni-Co samples and dislocation substructures in oxide samples were found in [153, 156]. Further studies are necessary to elucidate common patterns of superplasticity in nanostructures.

5. Conclusion

Our analysis of the most recent information on the strength of nanostructures comprising metals, alloys, and high-melting-point compounds permits us to state the topical problems in this field as follows:

- elucidation of the deformation and destruction mechanisms in nanoscale materials;
- investigations into the influence of size effects on the mechanical properties of nanostructures;
- studies of superplasticity mechanisms in nanomaterials.

Recent progress along these several avenues of research has enabled the formulation, even if in the first approximation, of theoretical concepts of nanomaterial strength and plasticity; moreover, new experimental data on the mechanical properties and superplasticity of these materials were obtained. However, the wide spectrum of available publications does not cover all aspects, requiring in-depth theoretical studies and extensive experimentation with the use of well-attested and representative samples. The ultimate goal of all the aforementioned research is to elucidate the nature of interfaces in nanoscale materials and develop methods for the manipulation of their properties. On the one hand, implementation of this goal may help to overcome difficulties posed by intercrystallite brittleness of nanostructures. On the other hand, it would be a decisive contribution to the optimization of the composition of superplastic nanomaterials and their processing procedures. Future studies should involve a much wider range of complex nanostructures with various types of boundaries separating not only ordinary grains and plates but also nanotubes (rods, plates), triple junctions, and segregations.

We note that a deeper insight into the boundary characteristics in nanoscale materials will greatly contribute to the progress of material science at large and its different aspects, such as embrittlement, aging, corrosion degradation, recrystallization, segregation, and diffusion in ordinary coarse-grained materials (see [159–163]).

The present review does not cover all varieties of nanomaterials. The strength of carbon nanostructures and related materials are analyzed at greater length in recent review [23], and biological, polymeric, and amorphous nanostructured objects require special consideration beyond the scope of this publication (see, e.g., [164–167]).

The authors are grateful to Yu A Osip'yan for his interest in this work and for the enlightening discussions. Financial support of RFBR the (grants 08-02-11001, 08-03-00105, and 06-02-17075) is acknowledged. RA thanks V V Klyucharev and S V Klyucharev for assistance and the RAS Presidium Programs P-18 and P-27 for support.

References

1. Morris D G *Mechanical Behaviour of Nanostructured Materials* (Uetikon-Zuerich, Switzerland: Trans Tech, 1998)
2. Gleiter H *Acta Mater.* **48** 1 (2000)
3. Andrievskii R A, Glezer A M *Fiz. Met. Metalloved.* **89** (1) 91 (2000) [*Phys. Met. Metallogr.* **89** 83 (2000)]
4. Valiev R Z, Islamgaliev R K, Alexandrov I V *Prog. Mater. Sci.* **45** 103 (2000)
5. Gutkin M Yu, Ovid'ko I A *Defekty i Mekhanizmy Plastichnosti v Nanostrukturnykh i Nekristallicheskikh Materialakh* (Defects and Mechanisms of Plasticity in Nanostructured and Non-Crystalline Materials) (St. Petersburg: Yanus, 2001)
6. Pozdnyakov V A, Glezer A M *Fiz. Tverd. Tela* **44** 705 (2002) [*Phys. Solid State* **44** 732 (2002)]
7. Noskova N I, Mulyukov R R *Submikrokristallicheskie i Nanokristallicheskie Metally i Splavy* (Submicrocrystalline and Nanocrystalline Metals and Alloys) (Ekaterinburg: UrO RAN, Inst. Fiziki Metallov, 2003)
8. Gutkin M Yu, Ovid'ko I A *Fizicheskaya Mekhanika Deformiruemykh Nanostruktur* Vol. 1 *Nanokristallicheskie materially* (Physical Mechanics of Deformable Nanostructures Vol. 1 Nanocrystalline Materials) (St. Petersburg: Yanus, 2003)
9. Kumar K S, Van Swygenhoven H, Suresh S *Acta Mater.* **51** 5743 (2003)
10. Estrin Y, Kim H S, in *Encyclopedia of Nanoscience and Nanotechnology* Vol. 8 (Ed. H S Nalwa) (Stevenson Ranch, Calif.: American Science Publishers, 2004) p. 489
11. Wolf D et al. *Acta Mater.* **53** 1 (2005)
12. Andrievskii R A, Ragulya A V *Nanostrukturnye Materialy* (Nanostructured Materials) (Moscow: Akademiya, 2005)
13. Gutkin M Yu, Ovid'ko I A *Fizicheskaya Mekhanika Deformiruemykh Nanostruktur* Vol. 2 *Nanosloinye Struktury i Pokrytiya* (Physical Mechanics of Deformable Nanostructures Vol. 2 Nanolayered Structures and Coatings) (St. Petersburg: Yanus, 2005)
14. Pozdnyakov V A, Glezer A M *Fiz. Tverd. Tela* **47** 793 (2005) [*Phys. Solid State* **47** 817 (2005)]
15. Meyers M A, Mishra A, Benson D J *Prog. Mater. Sci.* **51** 427 (2006)
16. Ma E *JOM* **58** (4) 49 (2006)
17. Glezer A M *Deformatsiya Razrushenie Mater.* (9) 30 (2006)
18. Chuvil'deev V N et al. *Stabil'nost' Struktury Nano- i Mikrorkristallicheskikh Materialov, Poluchennykh Metodami Intensivnogo Plasticheskogo Deformirovaniya* (Stability of the Structure of Nano- and Microcrystalline Materials Fabricated by Intense Plastic Deformation) (Nizhnii Novgorod: Izd. NNGU, 2006)
19. Van Swygenhoven H, Weertman J R *Mater. Today* **9** (5) 24 (2006)
20. Kolobov Yu R, Ivanov K V *Mater. Sci. Forum* **503–504** 141 (2006)
21. Valiev R Z, Aleksandrov I V *Ob'emnye Nanostrukturnye Metallicheskie Materialy: Poluchenie, Struktura i Svoistva* (Nanostructured Bulk Metallic Materials: Manufacture, Structure and Properties) (Moscow: Akademkniga, 2007)
22. Malygin G A *Fiz. Tverd. Tela* **49** 961 (2007) [*Phys. Solid State* **49** 1013 (2007)]
23. Eletskii A V *Usp. Fiz. Nauk* **177** 233 (2007) [*Phys. Usp.* **50** 225 (2007)]
24. Pozdnyakov V A *Izv. Ross. Akad. Nauk Fiz.* **71** 1751 (2007) [*Bull. Russ. Acad. Sci. Phys.* **71** 1708 (2007)]
25. Koch C C *J. Mat. Sci.* **42** 1403 (2007)
26. Dao M et al. *Acta Mater.* **55** 4041 (2007)
27. Koneva N A, Zhdanov A N, Kozlov E V *Izv. Ross. Akad. Nauk Fiz.* **70** 577 (2006) [*Bull. Russ. Acad. Sci. Phys.* **70** 663 (2006)]
28. Müller M, Albe K *Acta Mater.* **55** 3237 (2007)
29. Andrievskiy R A *Usp. Khim.* **66** 57 (1997) [*Russ. Chem. Rev.* **66** 53 (1997)]
30. Glezer A M *Izv. Ross. Akad. Nauk Fiz.* **67** 810 (2003) [*Bull. Russ. Acad. Sci. Phys.* **67** 893 (2003)]
31. Sauvage X, Wetscher F, Pareige P *Acta Mater.* **53** 2127 (2005)
32. Gryaznov V G et al. *Phys. Rev. B* **44** 42 (1991)
33. Andrievskii R A, Kalinnikov G V, Shtanskii D V *Fiz. Tverd. Tela* **42** 741 (2000) [*Phys. Solid State* **42** 760 (2000)]
34. Gutkin M Yu, Ovid'ko I A *Appl. Phys. Lett.* **88** 211901 (2006)
35. Gutkin M Yu, Ovid'ko I A *Fiz. Tverd. Tela* **50** 630 (2008) [*Phys. Solid State* **50** 655 (2008)]
36. Schiøtz J, Di Tolla F D, Jacobson K W *Nature* **391** 561 (1998)
37. Zhou Y et al. *Scr. Mater.* **48** 825 (2003)
38. Madan A, Barnett S A, in *Materials Science of Carbides, Nitrides, and Borides* (Eds Y G Gogotsi, R A Andrievski) (Dordrecht: Kluwer Acad. Publ., 1999) p. 187
39. Ievlev V M, Bugakov A V, Trofimov V I *Rost i Substruktura Kondensirovannykh Plenok* (Growth and Substructure of Condensed Films) (Voronezh: Isd. VGTU, 2000)
40. Spaepen F *Acta Mater.* **48** 31 (2000)
41. Lu L et al. *Science* **304** 422 (2004)
42. Zhang X et al. *Acta Mater.* **52** 995 (2004)
43. Shen Y F et al. *Scr. Mater.* **52** 989 (2005)
44. Conrad H *Nanotechnology* **18** 325701 (2007)
45. Phaniraj M P, Prasad M J N V, Chokshi A H *Mater. Sci. Eng. A* **463** 231 (2007)
46. Dubrovinskaia N et al. *Appl. Phys. Lett.* **90** 101912 (2007)
47. Shen T D et al. *Acta Mater.* **55** 5007 (2007)
48. Mayrhofer P H et al. *Prog. Mater. Sci.* **51** 1032 (2006)
49. Karpov M I, Vnukov V I, Volkov K G *Materialovedenie* (1) 48 (2004)
50. Karpov M I et al. *Deformatsiya Razrushenie Mater.* (6) 18 (2008)
51. Zhu B et al. *Acta Mater.* **53** 4825 (2005)
52. Malygin G A *Fiz. Tverd. Tela* **50** 1013 (2008) [*Phys. Solid State* **50** 1056 (2008)]
53. Koch C C *Scr. Mater.* **49** 657 (2003)
54. Zhang X et al. *Acta Mater.* **50** 4823 (2002)
55. Karimpoor A A et al. *Scr. Mater.* **49** 651 (2003)
56. Cheng S et al. *Acta Mater.* **53** 1521 (2005)
57. Farkas D *Met. Mater. Trans. A* **38** 2168 (2007)
58. Wang Y et al. *Nature* **419** 912 (2002)
59. Valiev R Z et al. *J. Mater. Res.* **17** 5 (2002)
60. Gil Sevillano J, Aldazabal J *Scr. Mater.* **51** 795 (2004)
61. Pozdnyakov V A *Pis'ma Zh. Tekh. Fiz.* **33** (23) 36 (2007) [*Tech. Phys. Lett.* **33** 1004 (2007)]
62. Malygin G A *Fiz. Tverd. Tela* **50** 990 (2008) [*Phys. Solid State* **50** 1032 (2008)]
63. Pokropivny V V, Skorokhod V V *Mater. Sci. Eng. C* **27** 990 (2007)
64. Shtremel' M A *Prochnost' Splavov* Pt. 1 *Defecty reshetki* (Strength of Alloys Pt. 1 Lattice Defects) (Moscow: MISIS, 1999)
65. Zhao Y H et al. *Apll. Phys. Lett.* **89** 121906 (2006)
66. Koch C C et al. *MRS Bull.* **24** (2) 54 (1999)
67. Karch J, Birringer R, Gleiter H *Nature* **330** 556 (1987)
68. Siegel R W, Fougere G E *Nanostruct. Mater.* **6** 205 (1995)
69. Morris M A, Leboeuf M *Mater. Sci. Eng. A* **224** 1 (1997)
70. Ma K J, Bloyce A *Surf. Eng.* **11** 71 (1995)
71. Han X D et al. *Nano Lett.* **7** 452 (2007)
72. Han X D et al. *Adv. Mater.* **19** 2112 (2007)
73. Zhang Y et al. *Adv. Funct. Mater.* **17** 3435 (2007)
74. Glezer A M, Manaenkov S E, Permyakova I E *Izv. Ross. Akad. Nauk Fiz.* **71** 1745 (2007) [*Bull. Russ. Acad. Sci. Phys.* **71** 1702 (2007)]
75. Pozdnyakov V A *Fiz. Met. Metalloved.* **97** (1) 9 (2004) [*Phys. Met. Metallogr.* **97** 7 (2004)]
76. Glezer A M, Permyakova I E, Manaenkov S E *Izv. Ross. Akad. Nauk. Fiz.* **72** 1335 (2008) [*Bull. Russ. Acad. Sci. Phys.* **72** 1265 (2008)]

77. Szlufarska I, Nakano A, Vashishta P *Science* **309** 911 (2005)
78. Noskova N I *Phys. Met. Metallogr.* **94** (Suppl. 1) 119 (2002)
79. Veprek S, Argon A S *J. Vac. Sci. Technol. B* **20** 650 (2002)
80. Andrievski R A *Surf. Coat. Technol.* **201** 6112 (2007)
81. Cavaleiro A, de Hosson J Th M (Eds) *Nanostructured Coatings* (New York: Springer, 2006)
82. Glezer A, Pozdnyakov V *Nanostruct. Mater.* **6** 767 (1995)
83. Kolesnikova A L, Ovid'ko I A, Romanov A E *Pis'ma Zh. Tekh. Fiz.* **33** (15) 26 (2007) [*Tech. Phys. Lett.* **33** 641 (2007)]
84. Malygin G A *Fiz. Tverd. Tela* **49** 2161 (2007) [*Phys. Solid State* **49** 2266 (2007)]
85. Bobylev S V, Ovid'ko I A *Fiz. Tver. Tela* **50** 617 (2008) [*Phys. Solid State* **50** 642 (2008)]
86. Mitra R, Ungar T, Weertman J R *Trans. Ind. Inst. Met.* **58** 1125 (2005)
87. Andrievski R A, Spivak I I *Prochnost' Tugoplavkikh Soedinenii i Materialov na Ikh Osnove* (Strength of High-Melting-Point Compounds and Materials Comprising Them) (Chelyabinsk: Metallurgiya, 1989)
88. Andrievski R A, in *Functional Gradient Materials and Surface Layers Prepared by Fine Particles Technology* (Eds M-I Baraton, I Uvarova) (Dordrecht: Kluwer Acad. Publ., 2002) p. 17
89. Ovid'ko I A, Sheinerman A G *Fiz. Tverd. Tela* **50** 1002 (2008) [*Phys. Solid State* **50** 1044 (2008)]
90. Morozov N F et al. *Dokl. Ross. Akad. Nauk* **406** 480 (2006) [*Dokl. Phys.* **51** 69 (2006)]
91. Hanlon T, Kwon Y-N, Suresh S *Scr. Mater.* **49** 675 (2003)
92. Glezer A M et al. *Mekhanicheskoe Povedenie Amorfnykh Splavov* (Mechanical Behaviour of Amorphous Alloys) (Novokuznetsk: SibGIU, 2006)
93. Mohamed F A *Acta Mater.* **51** 4107 (2003)
94. Chuvildeev V N et al. *Dokl. Ross. Akad. Nauk* **396** 332 (2004) [*Dokl. Phys.* **49** 296 (2004)]
95. Orlova T S et al. *Fiz. Tverd. Tela* **47** 820 (2005) [*Phys. Solid State* **47** 845 (2005)]
96. Kurlov A S, Gusev A I *Pis'ma Zh. Tekh. Fiz.* **33** (19) 46 (2007) [*Tech. Phys. Lett.* **33** 828 (2007)]
97. Utyashev F Z, Raab G I *Fiz. Met. Metalloved.* **104** 605 (2007) [*Phys. Met. Metallogr.* **104** 582 (2007)]
98. Li Y S, Tao N R, Lu K *Acta Mater.* **56** 230 (2008)
99. Glezer A M, Pozdhyakov V A *Dokl. Ross. Akad. Nauk* **398** 756 (2004) [*Dokl. Phys.* **49** 570 (2004)]
100. Pozdnyakov V A, Glezer A M *Izv. Ross. Akad. Nauk Fiz.* **68** 1449 (2004) [*Bull. Russ. Acad. Sci. Phys.* **68** 1621 (2004)]
101. Perevezentsev V N, Sarafanov G F *Fragmentatsiya pri Plasticheskoi Deformatsii Metallov* (Fragmentation in Plastic Deformation of Metals) (Nizhnii Novgorod: NNGU, 2007)
102. Glezer A M *Izv. Ross. Akad. Nauk. Fiz.* **71** 1764 (2007) [*Bull. Russ. Acad. Sci. Phys.* **71** 1722 (2007)]
103. Gunderov D V et al. *Deformatsiya Razrushenie Mater.* (4) 22 (2006)
104. Abrosimova G E et al. *Fiz. Tver. Tela* **49** 983 (2007) [*Phys. Solid State* **49** 1034 (2007)]
105. Glezer A M et al. *Mater. Sci. Forum* **584 – 586** 227 (2008)
106. Chaim R, Hefetz M *J. Mater. Sci.* **39** 3057 (2004)
107. Latapie A, Farkas D *Scr. Mater.* **48** 611 (2003)
108. Wu B, Heidelberg A, Boland J J *Nature Mater.* **4** 525 (2005)
109. Chen C Q et al. *Phys. Rev. Lett.* **96** 075505 (2006)
110. Wang G, Li X *Appl. Phys. Lett.* **91** 231912 (2007)
111. Ivanova E A, Indeitsev D A, Morozov N F *Dokl. Ross. Akad. Nauk* **410** 754 (2006) [*Dokl. Phys.* **51** 569 (2006)]
112. Golovin Yu I *Vvedenie v Nanotekhniku* (Introduction to Nanotechnology) (Moscow: Mashinostroenie, 2007)
113. Andrievskii R A et al. *Fiz. Tverd. Tela* **42** 1624 (2000) [*Phys. Solid State* **42** 1671 (200)]
114. Andrievskii R A et al. *Fiz. Tverd. Tela* **39** 1859 (1997) [*Phys. Solid State* **39** 1661 (1997)]
115. Andrievski R A *MRS Symp. Proc.* **501** 149 (1998)
116. Shtanskii D V et al. *Fiz. Tverd. Tela* **45** 1122 (2003) [*Phys. Solid State* **45** 1177 (2003)]
117. Musil J, in *Nanostructured Coatings* (Eds A Cavaleiro, J Th M de Hosson) (New York: Springer, 2006) p. 407
118. Musil J, Jirout M *Surf. Coat. Technol.* **201** 5148 (2007)
119. Li D J et al. *Appl. Phys. Lett.* **91** 251908 (2007)
120. Zhang S et al. *Surf. Coat. Technol.* **198** 74 (2005)
121. Chen J, Bull S J *Thin Solid Films* **494** 1 (2006)
122. Chen J, Bull S J *J. Phys. D Appl. Phys.* **40** 5401 (2007)
123. Glezer A M, Permyakova I E, Manaenkov S E *Dokl. Ross. Akad. Nauk* **418** 181 (2008) [*Dokl. Phys.* **53** 8 (2008)]
124. Choi S M, Awaji H *Sci. Technol. Adv. Mater.* **6** 2 (2005)
125. Andrievskii R A *Materialovedenie* (4) 20 (2006)
126. Sherif El-Eskandarany M *J. Alloys Comp.* **296** 175 (2000)
127. Sherif El-Eskandarany M *J. Alloys Comp.* **391** 228 (2005)
128. Basu B, Lee J-H, Kim D-Y *J. Am. Ceram. Soc.* **87** 317 (2004)
129. Carroll L, Sternitzke M, Derby B *Acta Mater.* **44** 4543 (1996)
130. Zhan G-D et al. *Mater. Sci. Eng. A* **356** 443 (2003)
131. Zhang S et al. *Surf. Coat. Technol.* **198** 2 (2005)
132. Botvina L R et al. *Ross. Nanotekhnol.* **2** (1–2) 106 (2007)
133. Smirnov B I, Shpeizman V V, Nikolaev V I *Fiz. Tverd. Tela* **47** 816 (2005) [*Phys. Solid State* **47** 840 (2005)]
134. Shpeizman V V et al. *Fiz. Tverd. Tela* **49** 644 (2007) [*Phys. Solid State* **49** 678 (2007)]
135. Andrievski R A, Anisimova I A, Anisimov V P *Thin Solid Films* **205** 171 (1991)
136. Mayrhofer P H et al. *Appl. Phys. Lett.* **83** 2049 (2003)
137. Andrievskiy R A *Usp. Khim.* **71** 967 (2002) [*Russ. Chem. Rev.* **71** 853 (2002)]
138. Veprek S et al. *Thin Solid Films* **476** 1 (2005)
139. Dalla Torre F et al. *Scr. Mater.* **53** 23 (2005)
140. Domínguez-Dodríguez A et al. *Scr. Mater.* **56** 89 (2007)
141. Yamakov V et al. *Acta Mater.* **50** 61 (2002)
142. Chokshi A H *Scr. Mater.* **48** 791 (2003)
143. Kottada R S, Chokshi A H *Scr. Mater.* **53** 887 (2005)
144. Chokshi A H *Mater. Sci. Eng. A* **483 – 484** 485 (2008)
145. Wei Y, Bower A F, Gao H *Acta Mater.* **56** 1741 (2008)
146. Wang N et al. *Acta Met. Mater.* **43** 519 (1995)
147. Kolobov Yu R et al. *Zernogranichnaya Diffuziya i Svoistva Nanostrukturnykh Materialov* (Grain-Boundary Diffusion and Properties of Nanostructured Materials) (Eds Yu R Kolobov, R Z Valiev) (Novosibirsk: Nauka, 2001)
148. Chuvil'deev V N et al. *Dokl. Ross. Akad. Nauk* **410** 335 (2006) [*Dokl. Phys.* **51** 500 (2006)]
149. McFadden S X et al. *Nature* **398** 684 (1999)
150. Valiev R Z et al. *Philos. Mag. A* **81** 25 (2001)
151. Padmanabhan K A, Gleiter H *Mater. Sci. Eng. A* **381** 28 (2004)
152. Zhou X et al. *Mater. Sci. Eng. A* **394** 353 (2005)
153. Wang G F, Chan K C, Zhang K F *Scr. Mater.* **54** 765 (2006)
154. Xu X et al. *Acta Mater.* **54** 255 (2006)
155. Kawasaki M et al. *Metalurg. Mater. Trans. A* **38** 1891 (2007)
156. Hiraga K et al. *Sci. Technol. Adv. Mater.* **8** 578 (2007)
157. Valiev R Z, Islamgaliev R K, Semenova I P *Mater. Sci. Eng. A* **463** 2 (2007)
158. Myshlyaev M M, in *Nanostrukturnye Materially — 2008: Belarus' — Rossiya — Ukraina* (Nanostructured Materials — 2008: Belarus – Russia – Ukraine) (Eds P A Vityazya et al.) (Minsk: Belorus. Nauka, 2008) p. 185
159. Gorelik S S, Dobatkin S V, Kaputkina L M *Rekristallizatsiya Metallov i Splavov* (Recrystallization in Metals and Alloys) (Moscow: MISIS, 2005)
160. Chuvil'deev V N *Neravnovesnye Granitsy Zeren v Metallakh. Teoriya i Prilozheniya* (Non-Equilibrium Grain Boundaries in Metals. The Theory and Applications) (Moscow: Fizmatlit, 2004)
161. Nechaev Yu S *Izv. Ross. Akad. Nauk Fiz.* **65** 1507 (2001) [*Bull. Russ. Acad. Sci. Phys.* **65** 1639 (2001)]
162. Nechaev Yu S *Solid State Phenom.* **138** 91 (2008)
163. Nechaev Yu S *Usp. Fiz. Nauk* **178** 709 (2008) [*Phys. Usp.* **51** 681 (2008)]
164. Bao G, Suresh S *Nature Mater.* **2** 715 (2003)
165. Schuh C A, Hufnagel T C, Ramamurty U *Acta Mater.* **55** 4067 (2007)
166. Buehler M J *J. Mater. Sci.* **42** 8765 (2007)
167. Meyers M A et al. *Prog. Mater. Sci.* **53** 1 (2008)
168. Lu L et al. *Science* **323** 607 (2009)